Master's thesis

Medical physics

REAL-TIME MOTION AND DYNAMIC RECEIVER SENSITIVITY CORRECTION FOR CEST-MRI IN THE HUMAN BRAIN AT 7T

Sami Vilho Juhani Auno

2018

Supervisor: Associate Professor Wolfgang Bogner

Reviewers: Professor Sauli Savolainen

Deputy Chief Physicist Marjut Timonen

HELSINGIN YLIOPISTO

FYSIIKAN LAITOS

PL 64 (Gustaf Hällströmin katu 2)

00014 Helsingin yliopisto

HELSINGIN YLIOPISTO — HELSINGFORS UNIVERSITET — UNIVERSITY OF HELSINKI

Tiedekunta/Osasto — Fakultet/Sektion — Faculty	Laitos — Institution — Department
Faculty of Science	Department of Physics

Tekijä — Författare — Author
Sami Vilho Juhani Auno

Työn nimi — Arbetets titel — Title
Real-time motion and dynamic receiver sensitivity correction for CEST-MRI in the human brain at 7T

Oppiaine — Läroämne — Subject
Medical Physics

Työn laji — Arbetets art — Level	Aika — Datum — Month and year	Sivumäärä — Sidoantal — Number of pages
Master's thesis	Tammikuu 2018	41 s.

Tiivistelmä — Referat — Abstract

Chemical Exchange Saturation Transfer (CEST) is a novel Magnetic Resonance Imaging (MRI) technique that utilises exchange reactions between metabolites and tissue water to map metabolite concentration or tissue pH noninvasively. Similarly to Magnetic Resonance Spectroscopy (MRS), CEST is able to detect many endogenous metabolites, but unlike MRS, CEST is based on imaging and thus enjoys the speed of modern MR imaging. On the other hand, CEST also suffers from the same difficulties as MRI and MRS. One of the most common source of image artifacts in MRI is subject motion during imaging. Many different motion correction methods have been devised. Recently, a novel real-time motion correction system was developed for MRS. This method is based on volumetric navigators (vNav) that are performed multiple times interleaved with the parent measurement. Navigator image comparison, affine matrix calculation, and acquisition gradient correction to correct the field of view to match subject head motion are done online and in real-time.

The purpose of this thesis is to implement this real-time motion correction method to CEST-MRI and study its efficacy and correction potential in phantoms and in healthy volunteers on 7T MR scanner. Additionally, it is hypothesised that the vNav images may be used to correct for motion related receiver sensitivity (B_1^-) inhomogeneities. Glutamate was chosen as the metabolite of interest due to it being the most abundant neurotransmitter in the human brain and due to its involvement in both normal cognitive function as well as many brain pathologies. Since glutamate has an amine group, it undergoes chemical exchange with water and is thus a usable metabolite for CEST imaging.

A glutamate phantom was constructed to show the glutamate concentration sensitivity of CEST and to test and optimise the CEST sequence. Seven healthy volunteers were imaged over a period of two months. All but one volunteer were imaged more than once (2-4 times). Subjects were measured without voluntary head motion and with controlled left-right and up-down head movements. All measurements were performed with and without motion correction to test the motion and B_1^--correction methods. Additionally, three volunteers were measured with a dynamic CEST experiment to assess the reproducibility of CEST.

The real-time motion correction method was found to be able to correct for small, involuntary head movements. 18 % of the CEST maps measured without motion correction were found to have motion artifacts whereas the equivalent number for maps with motion correction was 0 % (4/22 maps versus 0/18 maps). Larger (>0.7° or >0.7 mm in one coregistration step), voluntary head movements could not be corrected adequately. The vNav images could be used to correct for B_1^--inhomogeneities. This was found to improve CEST spectra quality and to remove lateral inhomogeneities from the CEST maps. The reproducibility of the CEST-MRI could not be established, however dynamic CEST measurements were found to be stable with only small contrast fluctuation of 4 % between consecutive maps due to noise.

Avainsanat — Nyckelord — Keywords
CEST, MRI, motion correction, glutamate

Säilytyspaikka — Förvaringsställe — Where deposited
Kumpulan tiedekirjasto

Muita tietoja — Övriga uppgifter — Additional information

Nomenclature

B_0	Main magnetic field
B_1^+	Transmitted magnetic field
B_1^-	Received magnetic field
BM	Bloch-McConnell
CEST	Chemical Exchange Saturation Transfer
CS	Chemical Shift
EPI	Echo Planar Imaging, a fast imaging sequence
FE	Frequency Encoding
FID	Free Induction Decay
FOV	Field of View
FT	Fourier Transform
GRE	Gradient-Recalled Echo, acquisition where echo is produced by gradients
k-space	Data matrix that stores the intensity values of NMR signal
MRI	Magnetic Resonance Imaging
MRS	Magnetic Resonance Spectroscopy
MT	Magnetisation Transfer
MTR	Magnetisation Transfer Ratio
MTR_{asym}	MTR-asymmetry, one type of MTR
NMR	Nuclear Magnetic Resonance
PBS	Phosphate-Buffered Saline

PE	Phase Encoding
RF	Radio Frequency
ROI	Region of Interest
SNR	Signal to Noise Ratio
T_1	Longitudinal relaxation time
T_2	Transverse relaxation time
TE	Echo Time
TR	Repetition Time
vNav	Volumetric Navigator
Z-value	Normalised image intensity value as a function of saturation offset frequency

Contents

1 Introduction

Magnetic Resonance Imaging (MRI) is a noninvasive imaging modality widely used in modern medicine. Since its inception by Nobel laureates Paul Lauterbur and Peter Mansfield in 1973[1, 2] the use of MRI has become a staple of modern diagnostic medicine. Unlike some other widely used imaging modalities, most notably computed tomography (CT), MRI does not utilise ionising radiation for image formation but rather a strong magnetic field and radio frequency (RF) pulses. MRI has a superior soft tissue contrast compared to other imaging modalities and has thus become a gold standard for providing morphological information on wide variety of pathologies ranging from cervical spine trauma [3] to intracranial tumours [4].

In addition to morphological images, MR scanners can be used to probe the chemical profile of tissue with Magnetic Resonance Spectroscopy (MRS). Unlike MRI, MRS does not produce an image but rather a spectrum for each measured voxel. Although MRS, or Nuclear Magnetic Resonance (NMR) as it is called outside of medicine, is a much older technique than MRI [5], it is not as widely used in clinical practice. MRS is, however, an important tool for researchers in neurosciences and metabolomics.

During the early 2000, a new MRI method was proposed. This new method, just like MRS, could provide molecular information of tissue, but would be based on imaging rather than spectroscopy. This novel method was termed Chemical Exchange Saturation Transfer (CEST) [6]. The principle behind CEST is in the exchange of magnetisation through the exchange of labile functional groups or atoms between two or more molecular pools. The most well known form of CEST is the exchange of protons between a solute molecular pool and water pool. These kind of proton exchange reactions have been used by chemists and spectroscopists since the mid-1950s in NMR spectroscopy to investigate protein dynamics [7]. CEST entered the consciousness of medical imaging only in the late 90s or early 2000 [6]. Since then the research volume on CEST methodology and new, potential contrast agents for CEST has been ever increasing. CEST is reminiscent to another sequence already routinely used in clinical practice, called Magnetisation Transfer (MT) imaging. In MT imaging, two image sets are acquired: one with an off-resonance RF saturation pulse train before the image acquisition, and one without. The idea is that water bound to macromolecular matrix will saturate during the off-resonance irradiation, and since this bound water pool is coupled with the free water pool, the saturation

(magnetisation) is transferred to the water pool making it partially saturated depending on the degree of coupling. Comparing the saturated and unsatured images reveal areas with significant water-macromolecule interactions. [8, 9, 10].

Off-resonance presaturation is also utilised in CEST-MRI. Unlike in MT imaging, in CEST multiple images are acquired each with RF presaturation pulse trains with different saturation frequencies, in addition to the unsaturated image. The saturation frequencies are usually swept over a range of frequencies around both side of the water saturation frequency. Signal intensity in each voxel can then be studied as a function of saturation frequency. This allows to inspect magnetisation transfer effects as a function of saturation frequency. Just like in MT imaging, the effect of macromolecular MT can be seen, this time as a background. As protons in different molecules have different Larmor frequencies, this allows the indirect study of dilute molecular pools, not unlike in MRS, through their proton exchange with water.

The exchange mediated MT effect, or the CEST effect, depends on the concentration of the labile proton pool as well as the rate of proton exchange between the pools. Since the exchange rate is a function of parameters such as pH and temperature, CEST can be used to indirectly measure metabolite concentration and tissue pH [11, 12]. Metabolites that have already been used as CEST contrast agents include brain glutamate [11], glucose [13, 14], brain myo-inositol [15], cartilage glycosaminoglycan [16, 17], and muscle creatine [18]. Additionally CEST has already shown to produce useful contrast in imaging cancer metabolism and acidosis [19], epilepsy [20], Alzheimer's disease [21], and radiation necrosis and tumour progression [22].

In this thesis, glutamate is the metabolite of choice for CEST imaging. Glutamate is the most abundant excitatory neurotransmitter in the vertebrate nervous system. It is involved in normal cognitive functions as well as memory.[23] Abnormal glutamate concentrations in the brain have been associated with wide range of diseases, such as Alzheimer's disease [24], multiple sclerosis [25] and epilepsy [26]. Glutamate is an anion of amino acid glutamic acid and has NH_3^+ amine group. This amine group exhibits proton exchange with surrounding water and can thus be used as an endogenous CEST agent.

Since CEST imaging is based on MR imaging rather than spectroscopy, it enjoys the speed of MRI. As with MR in general, CEST also suffers from the same problems in addition to inherent difficulties in CEST-MRI. Patient movement during MR measurements is a major source of artifacts in MRI and MRS, and CEST is no exception.

Movement is especially problematic for CEST as it relies on comparison between images measured at different time points. This problem is further amplified as many potential neuropathologies for CEST increase the change of involuntary movements during imaging. Recently, a novel real-time motion correction methodology was devised for MRS imaging [27, 28, 29, 30]. This method is based on a navigator pulse sequence that acquires multiple volumetric images during the course of MRS experiment, compares the images in real time, and applies appropriate corrections to the localising gradients to correct for movements during the measurement.

The purpose of this thesis is to implement this real-time motion correction method to the CEST sequence and to assess its efficacy for CEST imaging. Additionally, it is hypothesised that the navigator images could be used to correct for motion related receiver sensitivity changes during the course of CEST experiment to further decreasing motion artifacts.

2 Theory

2.1 Magnetic Resonance Imaging

2.1.1 Principle of Nuclear Magnetic Resonance

MRI is based on a physical phenomenon known as Nuclear Magnetic Resonance. Nuclei that have a nonzero spin have an intrinsic magnetic moment. This magnetic moment interacts with an external magnetic fields. A substance consisting of nuclei with nonzero spin is polarised in the external magnetic field as a result of this interaction. The strength of polarisation depends on the nuclear species, the strength of the external magnetic field as well as temperature. For $\pm\frac{1}{2}$-spins, such as hydrogen-1 nuclei (proton), the fraction between spins at higher energy levels and lower energy levels follow a Boltzmann distribution [10]:

$$\frac{N_h}{N_l} = e^{-\frac{\Delta E}{kT}}. \tag{1}$$

Here N is the number of spins in higher (h) and lower (l) energy levels, k is the Boltzmann constant, T is the absolute temperature of the system, and ΔE is the energy difference between the two energy levels. The polarisation manifests as a magnetisation of the substance so that the magnetisation vector is aligned with the external magnetic field in thermal equilibrium. The strength of this magnetisation can be derived to be

approximately [10]

$$M_{\text{eq}} \approx \frac{\gamma^2 h^2 N_s B_0}{4kT}. \tag{2}$$

Here M_{eq} is the thermal equilibrium magnetisation, γ is the gyromagnetic ratio of the nucleus, h is the Planck's constant, N_s is the number of spins, and B_0 is the magnetic field strength experienced by the spins. This spin polarisation may be perturbed with electromagnetic fields that have a frequency matching the energy difference between the nuclear spin levels of the nuclei in question in the specific constant external magnetic field. This frequency is called the Larmor frequency of a nucleus and it is defined as

$$\omega_L = -\gamma B_0. \tag{3}$$

For most nuclei this frequency is in the radiofrequency range and therefore these perturbing electromagnetic fields are called radiofrequency (RF) pulses. The gyromagnetic ratio is specific to different nuclei. For example, the gyromagnetic ratio of a hydrogen nucleus, a proton, is $\gamma_p \approx 267.513 \cdot 10^6 \ \frac{\text{rad}}{\text{sT}}$. The magnetic field experienced by the nucleus depends on the external magnetic field and local magnetic fields produced by surrounding electron cloud. This phenomenon is called nuclear shielding and it causes a shift in the Larmor frequency, called a chemical shift (CS) (Figure 1). Nuclear shielding allows the differentiation of identical nuclei that are part of different molecules or functional groups since they have different surrounding electron density distributions. This is the basis of MRS and, consequently, the reason for the saturation frequency distribution that is utilised in CEST.

When nonzero spin nuclei in external magnetic field are perturbed with RF pulses, the nuclei transfer to a higher energy level and are thus said to be excited. After the RF exposure ends, the nuclei start to relax back to their initial state, the thermal equilibrium. This process is called longitudinal magnetic relaxation and it is characterised by a time constant T_1 (Figure 2). Additionally, the spins of the excited nuclei lose coherence of magnetisation during relaxation due to the interactions between the atoms and the molecules. This leads to deterioration of the transverse magnetisation (Figure 2). This phenomenon is known as transverse magnetic relaxation and it is characterised by a time constant T_2. In real NMR experiment, transverse magnetisation tends to relax faster than T_2 would suggest. This is mainly due to inhomogeneities in the magnetic field that may arise from intrinsic defects in the magnet itself or changes in the magnetic susceptibility

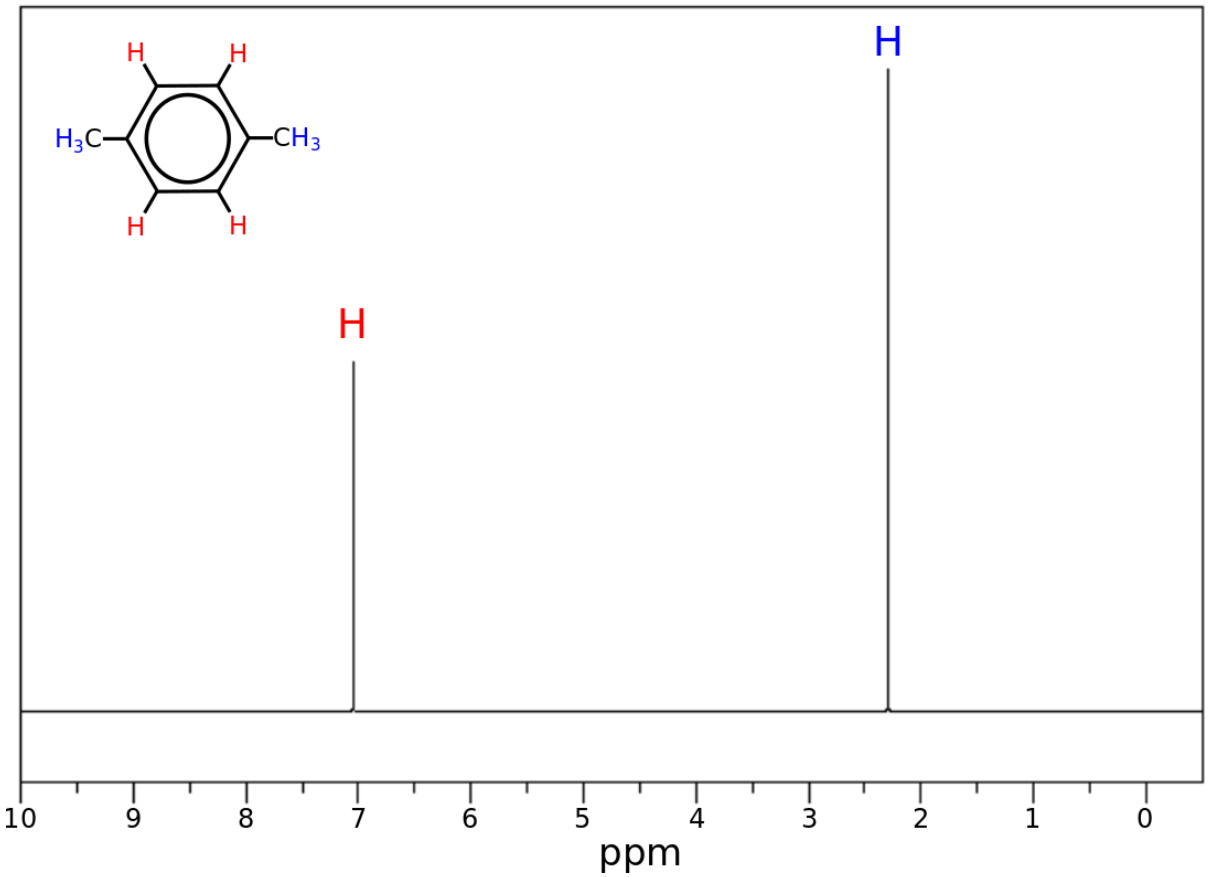

Figure 1: Example of one dimensional ^{1}H NMR spectrum of 1,4-dimethylbenzene demonstrating proton chemical shift due to differing chemical environments. The two peaks at 7.046 ppm and 2.296 ppm correspond to aromatic protons and methyl protons respectively. The difference in Larmor frequency is due to the difference in chemical environment that these nuclei experience. The aromatic protons are chemically equivalent to each other, as are the methyl protons, therefore only two peaks are seen. Data measured with JEOL 300 MHz (7.05 T) spectroscope. Solution: 0.02 ml : 0.5 ml $CDCl_3$. CS reference: Tetramethylsilane. Data adapted from Spectral Database for Organic Compounds SDBS [31].

of the measured material that induce distortions in the magnetic field. This observed transverse relaxation is called T_2* (T2-star).[10]

Mathematically the effect of relaxation of the magnetisation of spins can be described with macroscopic equations known as Bloch equations [32]. They describe the evolution of magnetisation with respect to time in presence of RF field and T_1 and T_2 relaxations. Usually the Bloch equations are written as a series of differential equations. A more concise way of writing them is in matrix form in the rotating frame of reference:

$$\frac{\mathrm{d}}{\mathrm{d}t}\vec{M} = A \cdot \vec{M} + \vec{C}, \tag{4}$$

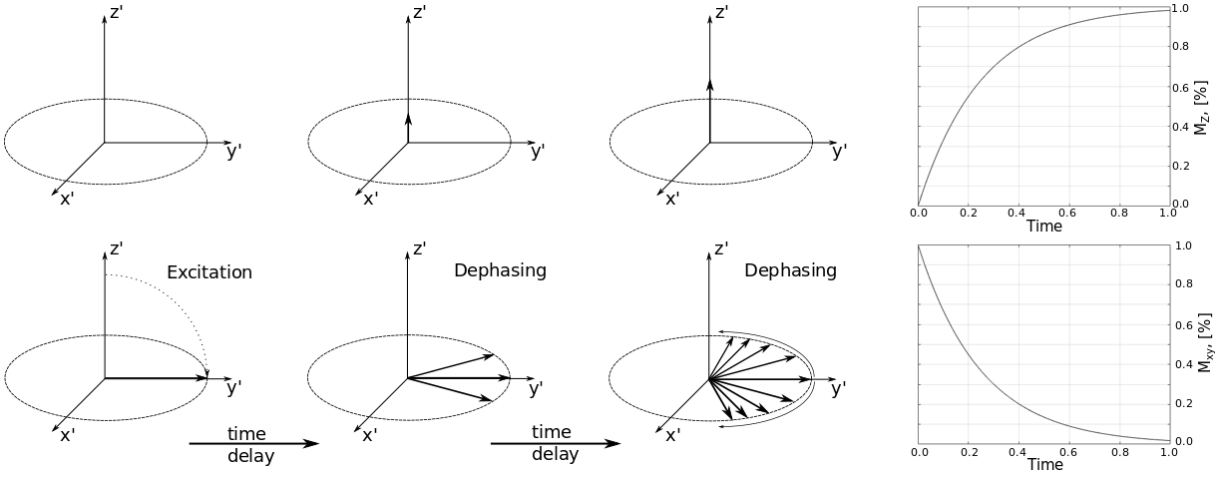

Figure 2: Sketches of the evolution of magnetisation of spin system after a 90° excitation pulse in rotating coordinate system. The top row shows the evolution of longitudinal magnetisation M_z. This relaxation is characterised by a time constant T_1. Bottom row shows how transverse magnetisation M_{xy} is lost due to the loss of coherence in a system of several spins.

where $\vec{M}$ is a vector that describes the nuclear magnetisation:

$$\vec{M} = \begin{bmatrix} M_x & M_y & M_z \end{bmatrix}^T, \tag{5}$$

A is a matrix that describes the system itself along with all the external influences the system experiences:

$$A = \begin{bmatrix} -R_2 & -\Delta\omega & 0 \\ +\Delta\omega & -R_2 & +\omega_1 \\ 0 & -\omega_1 & -R_1 \end{bmatrix}. \tag{6}$$

Here R_1 and R_2 are longitudinal and transverse relaxation rates, i.e. reciprocal of the corresponding times respectively. The quantity $\Delta\omega$ is the RF pulse frequency offset relative to the Larmor frequency of the nuclei of interest (ω_a). It is defined as

$$\Delta\omega = \omega_{\text{rf}} - \omega_a. \tag{7}$$

On resonance, the RF irradiation field $\vec{B}_1 = \begin{bmatrix} B_1 & 0 & 0 \end{bmatrix}^T$ induces a precession of the magnetisation with frequency $\omega_1 = \gamma B_1$ around the x-axis of the rotating frame of reference. Off resonance irradiation induces a precession around an effective field $\vec{B}_{\text{eff}}$ with a frequency $\vec{\omega}_{\text{eff}} = \begin{bmatrix} \omega_1 & 0 & \Delta\omega \end{bmatrix}^T$. Finally, the constant vector $\vec{C}$ is defined as

$$\vec{C} = \begin{bmatrix} 0 \\ 0 \\ R_1 M_0 \end{bmatrix}. \tag{8}$$

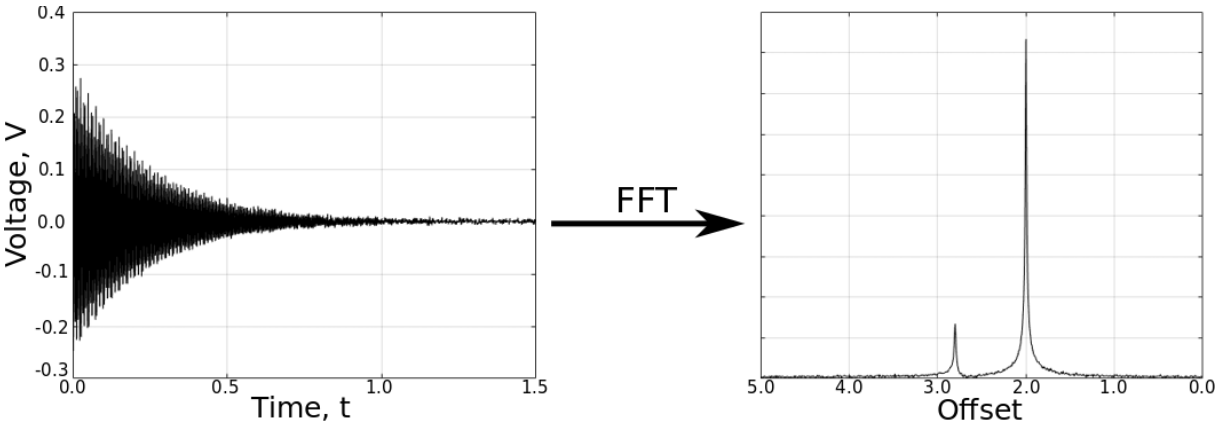

Figure 3: Applying Fast Fourier Transform (FFT) to the signal reveals the different frequencies that the signal contains. This is the basis of both NMR and MRI techniques. Here a simulated FID containing two different frequencies and some random noise is transformed into frequency domain. The units are arbitrary.

where M_0 is the transverse magnetisation at time $t = 0$.

Relaxation phenomena result not only from spins interacting with the external magnetic field, but also from spins interacting with other spins. Such interconnected spins are called spin systems and the spins are said to be coupled. There are different pathways for spins to interact and these pathways may be either inter- or intramolecular. These interactions may manifest as a transfer of excitation, or magnetisation, between different spins or molecules. These MT phenomena are widely used in NMR spectroscopy to map the relationships between spins within a molecule, for example with INEPT experiment. They may also be used to probe intermolecular connections.[33] MT effects are also used in clinical MRI to enhance water proton signal and map areas with significant water-macromolecule interactions.[8, 9] Here the coupling between large macromolecules and free water is utilised so that magnetisation is transferred from the macromolecular pool to water pool. These MT effects occur through multiple different pathways, most notably dipole-dipole interactions and proton exchange. The magnetisation transfer through the exchange of protons between pools may also be utilised alone. This is called Chemical Exchange Saturation Transfer.

2.1.2 Image formation

During relaxation, the precession of magnetisation in transverse plane can be used to generate a detectable signal by using external coils. Rotating magnetisation induces a

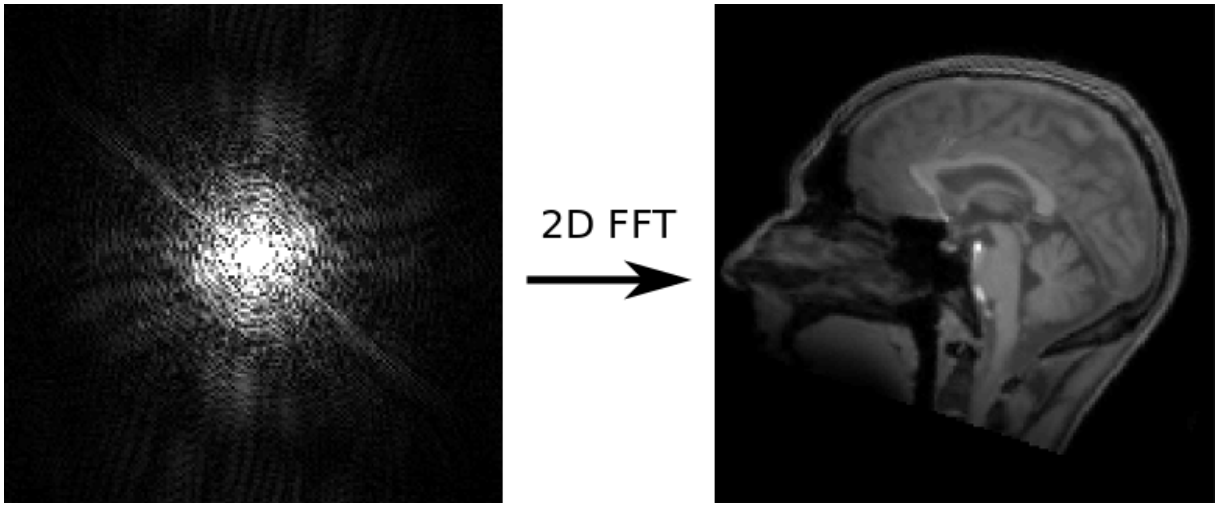

Figure 4: In imaging, a data matrix called k-space is filled with signal amplitudes as a function of time (left image). This matrix is traditionally filled line-by-line, but nowadays more efficient ways to fill the k-space have become more popular. The k-space is then transformed to image space (or frequency space, right image) by 2D FFT. Similarly 3D k-space would be transformed by 3D FFT.

current in the external coils. This signal is characterised by the strength of the external magnetic field, the chemical species and the nuclei in question, the initial state of the magnetisation before excitation RF pulse and the relaxation parameters of the material. In NMR, the signal is usually acquired right after an RF pulse. The signal begins strong and starts to decay due to T_2* relaxation. This form of signal is called Free Induction Decay (FID). In imaging it is more usual to acquire so called echoes where the signal starts in incoherent state and gradually becomes more coherent until full coherence is achieved. Then the signal decays just as in FID. In both cases the signal is then transformed from time-domain to frequency-domain by Fourier transform (FT) (Figure 3).

In addition to differentiating chemical species from each other, differences in Larmor frequency can also be used for localisation of signal. The external magnetic field can be made spatially dependent with external magnetic gradient coils and thus the signal frequency will have spatial dependency. This is the principle behind signal localisation in MRI. To create an image, a time domain data matrix, called k-space, is collected (Figure 4). The k-space is traditionally filled in line-by-line basis, each line being one measurement. The direction of the line in k-space is called the frequency-encoding (FE) direction and it corresponds to one physical dimension in the laboratory coordinate system. During the measurement of one line in k-space, a magnetic field gradient is applied along this

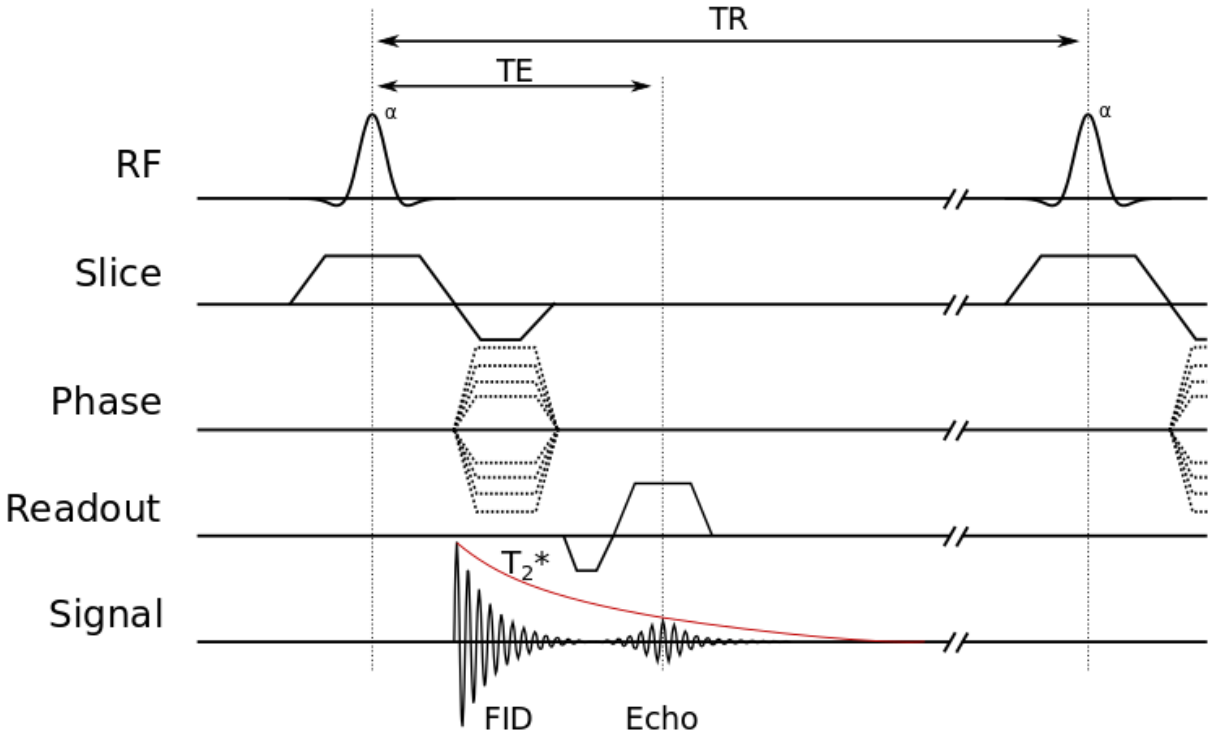

Figure 5: A pulse diagram of a simple gradient echo sequence (GRE) with linear readout gradients. The sequence starts with a radio frequency (RF) excitation pulse that flips the spins by an angle of α degrees. Simultaneously a slice selection gradient is applied to ensure that only spins of certain slice are excited. Then phase encoding gradient is applied. The strength and polarity of the phase encoding gradient is changed for each repetition. Readout gradient is applied during signal acquisition. Although Free Induction Decay (FID) is also formed, only the echo is acquired. The readout gradient ensures the spatial dependency of the frequency distribution of the echo signal. The time between the excitation pulse and the echo is characterised by time TE. This time can be changed by the operator by changing the strength of the readout gradients. The whole sequence is repeated for each line in k-space. The time between repetitions is called TR. This is also set by the operator. The signal decays exponentially by a characteristic time constant T_2*.

physical dimension. This gradient is called the frequency-encoding gradient. Another magnetic field gradient can be applied perpendicular to the FE gradient after the RF excitation but before the measurement of the signal. This gradient changes the phase of the signal and is thus called the phase-encoding (PE) gradient. The signal corresponds to a new line in k-space shifted along the second dimension, called the phase-encoding dimension. After the k-space has been filled, it is transformed to image space by applying a two-dimensional Fourier transform. Slice discrimination can be performed by applying a

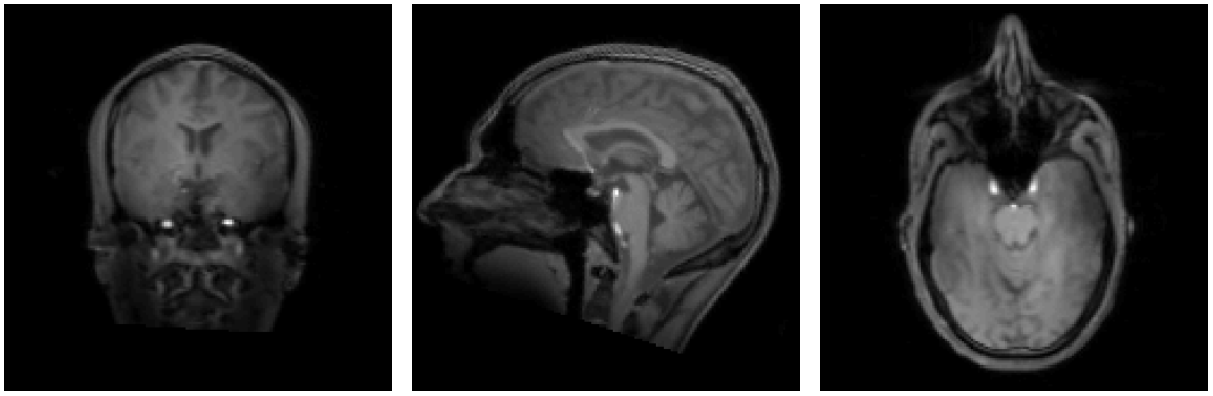

(a) (b) (c)

Figure 6: Example of MRI brain images showing coronal (a), sagittal (b), and transverse (c) slices. These images are from 3D TurboFLASH based auto-align sequence that is used for initial localisation and aligning the slice according to previous imaging sessions.

slice selection gradient and a shaped RF pulse so that only nuclei in that slice are excited ensuring that all signal originates only from this specific slice. Another way is to utilise a second PE gradient along the third dimension and fill a three-dimensional k-space. This is the basis of 3D imaging.

RF pulses and gradients are applied in a sequence, called a pulse sequence. Pulse sequences are often represented with pulse sequence diagrams (Figure 5). Pulse sequence diagrams show the applied pulses and gradients with respect to time. These sequences are read and applied by the MRI scanner.

2.2 Chemical Exchange Saturation Transfer

2.2.1 Introduction

The goal of CEST is to utilise the exchange of magnetisation between different molecular pools to receive information on chemical and physical properties of one or more of these pools. This is achieved, very much like in MT imaging, by off-resonance irradiation that selectively saturates one of the pools. This pool then transfers the saturation through chemical exchange to water pool (Figure 7). The stronger this transfer effect is, the more water saturates and the less signal is acquired with the subsequent imaging sequence. Unlike in MT imaging, the saturation frequency is changed during the course of the CEST experiment. This means that multiple images are acquired, each having been saturated with different saturation frequency preceding acquisition. Studying the intensity of each

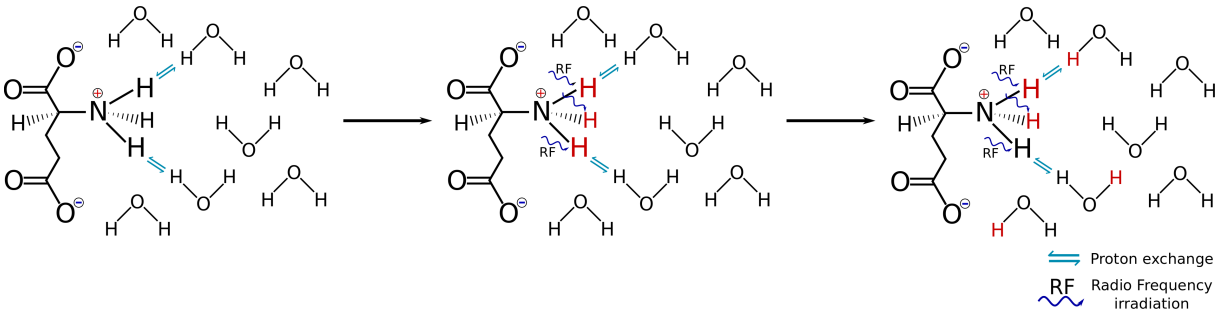

Figure 7: A diagram showing glutamate surrounded by water molecules. The glutamate molecule is constantly exchanging protons (double arrow) with the water molecules. When system is irradiated with radio frequency irradiation (squiggly arrow) that has a frequency matching the Larmor frequency of the amine protons of glutamate, the magnetisation of these protons saturate (red letter H). Due to the constant chemical exchange, these saturated protons will be exchanged with water. Gradually more and more water protons are also saturated even though they are not directly saturated.

voxel with respect to the saturation frequency reveals a spectrum that shows that the off-resonance saturation results in decrease of water signal intensity in very frequency specific way (Figure 10). Unlike in MRS, the zero ppm is assigned to water frequency. Most studied intrinsic metabolites have chemical shift of ± 3.5 ppm from water [34]. Glutamate amine protons are at 3 ppm whereas amines of small peptides and proteins express CEST effect around 2 ppm.

The evolution of magnetisation under chemical exchange can be described by so called Bloch-McConnell (BM) equations [36]. These are modified Bloch equations that also take into account exchange events. The simplest BM equations to model CEST have two pools, a water pool (pool a) and a dilute solute pool (pool b) in thermal equilibrium magnetisations M_{0a} and M_{0b}. These pools are interacting with each other solely through chemical exchange. The ratio of their equilibrium magnetisations, and consequently the ratio of their exchangeable protons, is $f_b = \frac{M_{0b}}{M_{0a}}$. Both pools have distinct resonance frequencies ω_a and ω_b respectively. The two pools exchange protons with forward (b $\rightarrow$ a) exchange rate k_b and backward exchange rate $k_a = f_b k_b$. Both pools have independent longitudinal and transverse relaxation rates $R_{1a/b} = (T_{1a/b})^{-1}$ and $R_{2a/b} = (T_{2a/b})^{-1}$ respectively. When the system is exposed to off-resonance external RF field $\vec{B}_1^+ = \left(B_1^+, 0, 0\right)$ with a frequency of ω_{RF}, precession is induced around an effective field $\vec{B}_{\text{eff}} = \left(\omega_1, 0, \Delta\omega\right)/\gamma$, where $\omega_1 = \gamma B_1^+$ and $\Delta\omega = \omega_{\text{RF}} - \omega_a$. As is convention

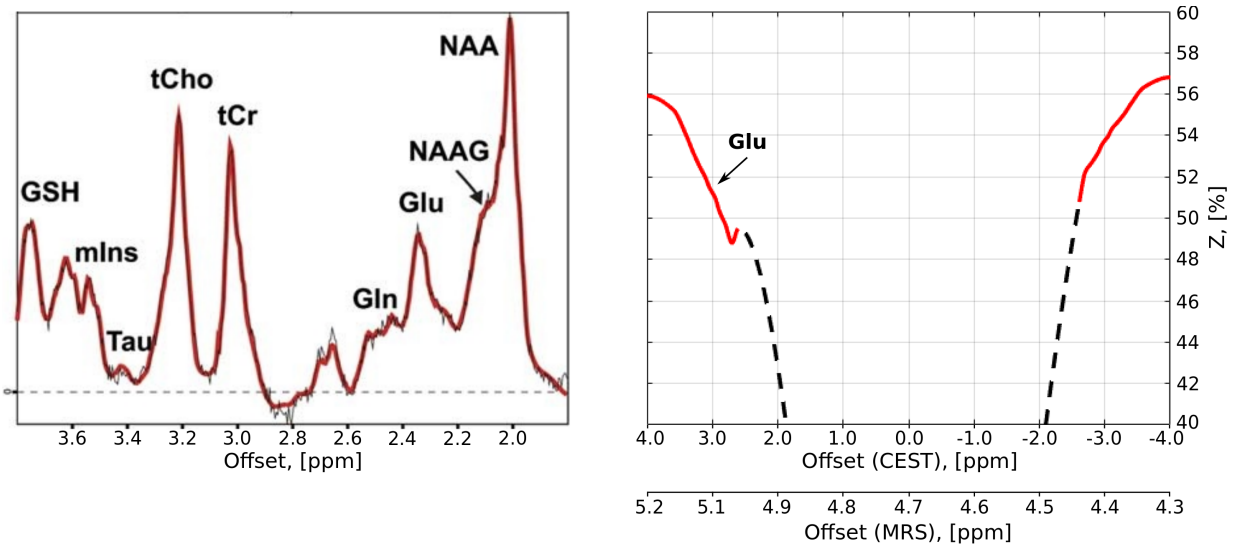

(a) (b)

Figure 8: Proton Magnetic Resonance Spectroscopy (MRS) (a) and Chemical Exchange Saturation Transfer (CEST) (b) spectra in the frontal lobe measured at 7T MR scanner. For the CEST spectrum, only offsets from ±4.0 to ±2.6 were measured (red line). The black dashed line is an extrapolation that assumes that Z = 0 at 0 ppm. Note the difference in chemical change (offset) between the two spectra. The MRS spectrum is referenced to tetramethylsilane at 0 ppm whereas the CEST spectrum is referenced to water which in MRS spectrum resonates at 4.7 ppm. Additionally, the glutamate peak (Glu) at *sim*2.35 ppm in the MRS spectrum comes from aliphatic C3 protons whereas the Glu peak at 3.0 ppm in the CEST spectrum (∼5.1 ppm in MRS spectrum) comes from amine protons. All the metabolites in the MRS spectrum manifest on the right hand side (upfield) of water peak. Another x-axis has been drawn under the CEST spectrum to emphasise the difference in offset referencing between the two methods. Reproduced (a) with kind permission from Gruber *et al* [35], copyright ©2017 Wolters Kluwer Health, Inc.

in CEST, 0 ppm is assigned to chemical shift of water, i.e. $\omega_a = 0$. For such system the BM equations may be written in matrix form as:

$$\frac{\mathrm{d}}{\mathrm{d}t}\vec{M} = A \cdot \vec{M} + \vec{C}, \tag{9}$$

This formula is very reminiscent of the original Bloch equations, only extended to include two different pools with some interaction terms. Here

$$\vec{M} = \begin{bmatrix} M_{xa} & M_{ya} & M_{za} & M_{xb} & M_{yb} & M_{zb} \end{bmatrix}^T \tag{10}$$

is the magnetisation vector containing x, y, and z magnetisation components of both pools

(a and b). Matrix A describes the system itself and contains both external (e.g. RF field) and internal (e.g. relaxation) as well as cross pool (i.e. exchange) interactions. Matrix A is a block matrix of form

$$A = \begin{bmatrix} L_a - K_a & +K_b \\ +K_a & L_b - K_b \end{bmatrix} \tag{11}$$

where L_i and K_i are 3×3 submatrices

$$L_i = \begin{bmatrix} -R_{2i} & -\Delta\omega_i & 0 \\ +\Delta\omega_i & -R_{2i} & +\omega_1 \\ 0 & -\omega_1 & -R_{1i} \end{bmatrix} \tag{12}$$

and

$$K_i = \begin{bmatrix} k_i & 0 & 0 \\ 0 & k_i & 0 \\ 0 & 0 & k_i \end{bmatrix}. \tag{13}$$

where $i = a, b$. Lastly, the constant vector $\vec{C}$ is

$$C = \begin{bmatrix} 0 & 0 & R_{1a}M_{0a} & 0 & 0 & R_{1b}M_{0b} \end{bmatrix}^T. \tag{14}$$

The BM equation can be extended to include nearly arbitrarily complex system of multiple pools. However, usable analytical solutions are hard to come by and exist only for small, simple systems [37]. The reason for this is that the size of the matrices depends on the number of pools. A formal solution to the BM equations is given as

$$\vec{M} = \left(\vec{M}_0 + A^{-1}\vec{C}\right) e^{A \cdot t} - A^{-1}\vec{C}, \tag{15}$$

where $\vec{M}_0$ is the system's magnetisation vector at time $t = 0$. As the number of pools increases, this solution becomes increasingly more computationally demanding. Therefore different analytical simplifications have been developed for two and three pool systems (an excellent review of different BM equations approximations can be found from paper by M. Zaiß and P. Bachert [34]).

Contrary to what the name would suggest, chemical exchange is not the only pathway for magnetisation transfer in CEST. Other notable pathways are different cross-relaxations, or nuclear Overhauser effects (NOE), that may occur directly between adjacent protons of the same (intramolecular) or different (intermolecular) molecule, or

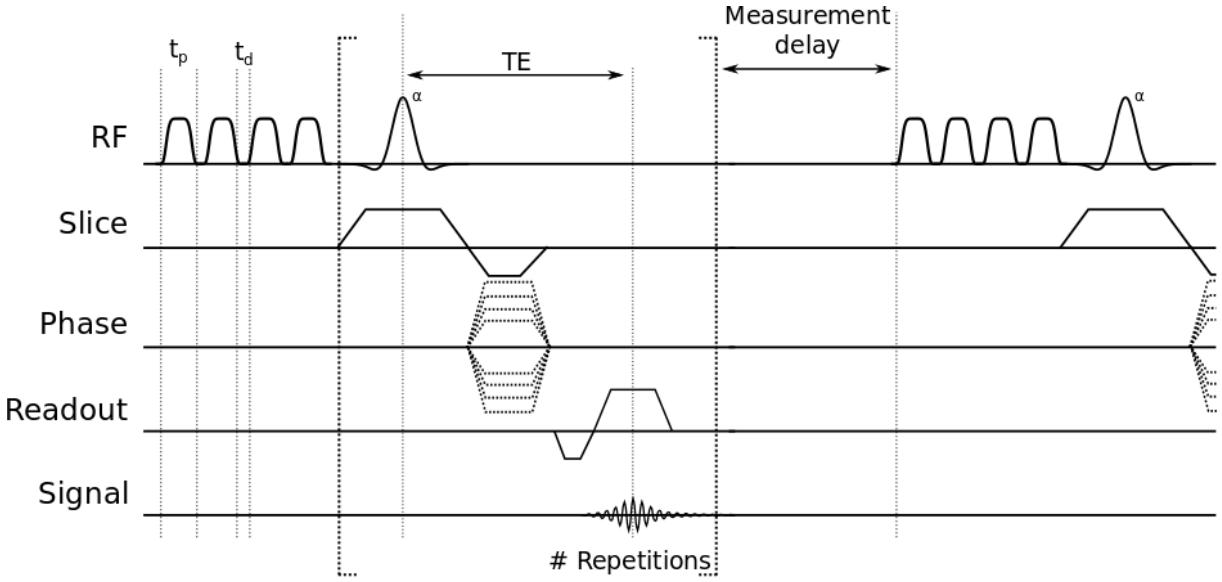

Figure 9: A pulse sequence diagram of a basic CEST pulse sequence. The sequence begins with a train of saturation pulses each with an amplitude of B_1^+ and length t_p. Each pulse is separated with a small delay of t_d. This pulse train is followed by a gradient echo acquisition sequence as described in Chapter 2.1.2. This is then repeated multiple times changing the frequency of the saturation pulses. There is a delay between consecutive measurements to let the magnetisation relax.

indirectly through exchange (exchange-relayed NOE) [38]. The effect of these pathways may be seen in the CEST spectrum. The frequencies where these pathways are the most evident may overlap with the saturation frequencies of the proton exchange reactions that are of interest and thus interpretation should be done cautiously. For example, aliphatic NOE usually manifests around -3.5 ppm whereas aromatic NOE around +3.5 ppm [39]. These may interfere with asymmetry analysis of amides (+3.5 ppm) or even glutamate (+3 ppm) as is explained later. Additionally if the exchangeable protons have Larmor frequency close to water, direct water saturation, also known as the spill-over effect, can further dilute the CEST effect making interpretation even more difficult.

A simple CEST experiment consists of a frequency selective saturation pulse train with pulse amplitude of B_1^+ and frequency ω_{RF} followed by signal acquisition. The number of saturation pulses in the pulse train, their length, and the delay between them are all operator specified parameters that affect the result. The frequency of the saturation pulses are then changed and the measurement is repeated (Figure 9). The actual number of measurements, their specific saturation frequencies and their distribution are also defined by the operator. By sweeping a range of saturation frequencies and measuring the

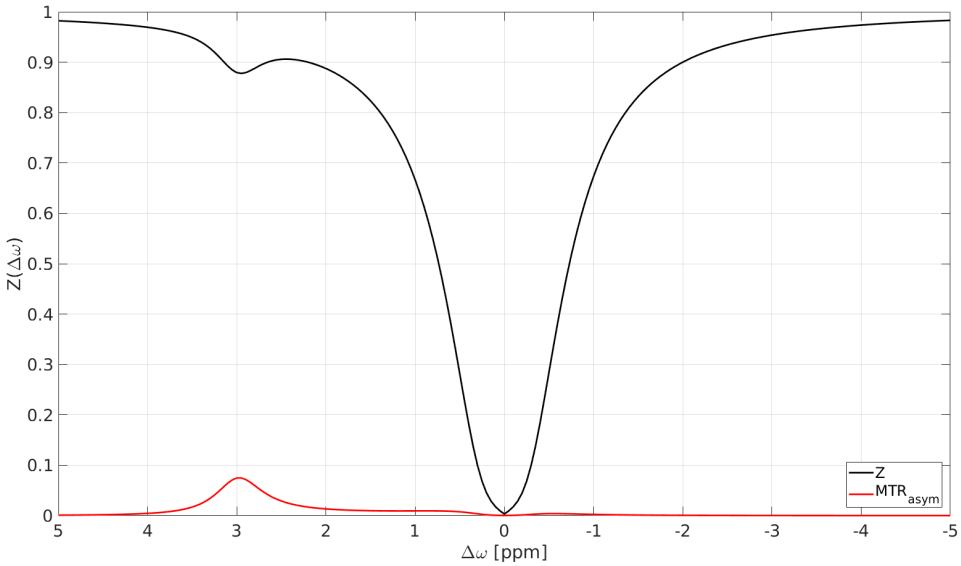

Figure 10: A simulated Z-spectrum with corresponding MTR asymmetry curve. The simulation was based on an analytical solution to the two pool Bloch-McConnell equations[40, 41]. A clear suppression (a "peak") can be seen around 3 ppm in the Z-spectrum (black line) corresponding to chemical exchange between water and some labile molecule. MTR asymmetry curve (red line) shows the corresponding effect as a peak. The simulation parameters were: $T_{1a} = 1.5$ s, $T_{2a} = 0.05$ s, $T_{1b} = 1$ s, $T_{2b} = 0.06$ s, $k_{ba} = 100$ s^{-1}, $f_b = 3 \cdot 10^{-3}$, $\omega_b = 3.0$ ppm, $B_0 = 300$ MHz, number of saturation pulses: 3, length of saturation pulses: 100 ms, duty cycle: 91%.

amplitude of water signal, a spectrum may be constructed. Additionally, usually at the beginning of the experiment, an image without presaturation is acquired. This is used to normalise the rest of the images so that

$$Z(\Delta\omega) = \frac{M(\Delta\omega)}{M_0}, \tag{16}$$

where $Z(\Delta\omega)$ is the normalised image stack, $M(\Delta\omega)$ are the unnormalised CEST images for each saturation frequency $\Delta\omega$, and M_0 is the unsaturated image. The resulting images can be compiled into a spectrum for each voxel. This is known as Z-spectrum (Figures 8 and 10).

2.2.2 Magnetisation Transfer Ratio

As such, the Z-spectrum is hard to interpret. Many different methods to quantify the Z-spectrum have been proposed [34]. One of the most used methods is to compare the different sides of the Z-spectrum around the water peak. This is known as the magnetisation transfer ratio asymmetry analysis (MTR_{asym}) [42]. The general shape of the Z-spectrum

is due to direct water saturation (spill over effect). If it is assumed that the spill over is symmetric around water, the CEST effect may be isolated by taking the difference between a reference Z-value (Z_{ref}) and exchange labelled Z-value where the reference is directly in opposite frequency to the labelled Z-value (Figure 10).

$$\mathrm{MTR}_{\mathrm{asym}}(\Delta\omega) = Z_{\mathrm{ref}}(\Delta\omega) - Z(\Delta\omega) \tag{17}$$

Although $\mathrm{MTR}_{\mathrm{asym}}$ has an inherent assumptions of independent contributions from water and solute pools, it is an adequate first approximation for the purpose of this thesis. From here on $\Delta\omega$ will be referred simply as offset.

2.3 Corrections

2.3.1 B_0-inhomogeneity correction

MTR-asymmetry depends on comparison between intensity values of known offsets. Saturation offset is linearly dependent on the strength of the external magnetic field (Equation 3). Therefore, even minor B_0-inhomogeneities change the MTR-asymmetry values and thus a B_0-inhomogeneity correction is necessary. Many different B_0 correction methods have been reported in the literature [42, 43, 44, 45, 46, 47]. In this study, the B_0 maps were determined from the CEST experiment itself. This was possible as the CEST sequence is based on dual-echo gradient echo (GRE) sequence [47].

In dual-echo GRE CEST a single CEST measurement produces two magnitude and two phase images with two different echo times. Between these two echoes, the phase of each voxel develops. The amount of phase accumulation is proportional to the echo time difference and the magnetic field inhomogeneity. The field maps are calculated by taking the difference between the two phase images (Φ_1 and Φ_2), and dividing by the echo time difference:

$$\Delta B_0(\Delta\omega) = \frac{\Phi_1(\Delta\omega) - \Phi_2(\Delta\omega)}{\gamma(\mathrm{TE}_1 - \mathrm{TE}_2)} \tag{18}$$

These field maps are then translated to ppm scale. The correction is applied by shifting each measurement point of Z-spectra in the x-axis according to the ppm-field map.

The strength of this method is that a field map is produced for each CEST measurement enabling dynamic B_0-inhomogeneity correction. Other methods, such as WASSR [43], rely on static B_0 field maps acquired before or after the CEST measurements.

2.3.2 B_1^+-inhomogeneity correction

Similarly to B_0-inhomogeneity, the transmit field, or B_1^+-inhomogeneity also affects the MTR-asymmetry analysis results. B_1^+, however, affects directly on the CEST effect by affecting the magnitude of the magnetisation transfer (Equations 11 and 12).

B_1^+-inhomogeneity correction was based on Z-B1-correction [48] where corrected Z-values are interpolated from pre-acquired flip angle maps. The flip angle mapping was performed with pre-saturation turbo-FLASH-based B_1^+-mapping sequence [49, 50]. The flip angle maps were used to calculate relative B_1^+ saturation maps ($B_{1\mathrm{rel}}^+$) and an actual B_1^+ map was then calculated by

$$B_1^+(x,y) = B_{1\mathrm{rel}}^+(x,y)B_{1\mathrm{nom}}^+ \tag{19}$$

where $B_{1\mathrm{nom}}^+$ was the nominal saturation amplitude chosen on the scanner. This B_1^+ map was then used to interpolate corrected Z-values (Z_{corr}) so that

$$Z_{\mathrm{corr}}(B_1^+,x,y) = a(x,y)B_1^+(x,y) + 1 \tag{20}$$

when assuming $Z_{\mathrm{corr}} = 1$ when $B_1^+ = 0$. Here a is a negative coefficient.

2.3.3 Motion correction

Subject motion during MR imaging has been problematic since the early days of the imaging modality. In fact, bulk motion is the most common source of imaging artifacts. [51, 52]

CEST quantification relies on image intensity comparison between two different saturation offsets acquired at different time points, sometimes several minutes apart (Section 2.2.2). Head movement during this time period may produce severe artifacts in the resulting maps. Motion artifacts may be alleviated retrospectively by image coregistration, but this works only in-plane. Retrospective respiratory gating has been utilised successfully in CEST previously [53], but naturally this is not applicable to non-respiratory related motion.

Volumetric EPI navigators (vNav) have been successfully utilised in MRS previously to correct for motion, shim, and frequency drift in real time [27, 28, 29] during measurement. The navigator produces a 3D image set covering the whole brain volume 17 for each offset measurement. The first vNav image set is used as a reference to which all

other vNav images are compared to. The correction algorithm calculates iteratively affine transformation matrix with respect to the first vNav image set taking into account translation and rotation. These are then applied to the vNav and the CEST sequence imaging gradients making the field of view follow the head pose in real-time. Additionally a log-file is produced that shows translation and rotation in sagittal, coronal, and transverse planes. The whole process of imaging and calculating corrections take approximately 300 ms and can therefore easily be fitted into the measurement.

Since the motion correction algorithm is an iterative process, large singular movements can result in imperfect correction. In these cases the vNav sequence is repeated immediately before CEST acquisition 11. Total translation and rotation are calculated by:

$$T_{tot} = \sqrt{T_x^2 + T_y^2 + T_z^2} \tag{21}$$

and

$$R_{tot} = \frac{180}{\pi} \cos^{-1}\left(\frac{R_x + R_y + R_z - 1}{2}\right) \tag{22}$$

respectively. Here T_i is the translation along axis i in mm, and R_i is the rotation around axis i in radians. The subscript i may be x, y, or z.

2.3.4 B_1^--inhomogeneity, or receiver sensitivity correction

In addition to motion related localisation artifacts, subject head movement can alter the receiver coil sensitivity due to head moving closer or further away from the coil elements. This causes a change in signal intensity, which can erroneously be interpreted as an exchange related signal change. Therefore it is important to correct such dynamic changes in the CEST images. The same intensity change is observed in the vNav images. Therefore it is possible to use these vNav images to calculate the relative intensity change and apply it to the CEST images retrospectively. Here it is assumed that this change is proportionally the same in both sequences.

The receiver sensitivity correction, or B_1^--inhomogeneity correction, is calculated by computing sensitivity maps from the navigator images. This is done by calculating the difference in intensity in the vNav images with respect to the first vNav image set in the experiment. These difference maps are then normalised by the first vNav image set. Since the navigator images have a different matrix size (32×32 vs. 128×128) and potentially also different field of view, the difference vNav images are then interpolated, smoothed,

and transformed into the same coordinate system as the parent CEST images (Figure 21c). The correction is calculated by

$$\mathbf{I}_{\text{corr}} = \mathbf{I}_{\text{i}} \circ (1 - \mathbf{S}) \tag{23}$$

where $\mathbf{I}_{\text{corr}}$, $\mathbf{I}_{\text{i}}$, and $\mathbf{S}$ are the B_1^--corrected CEST image matrix, the initial uncorrected matrix, and the interpolated sensitivity matrix respectively. Operator $\circ$ denotes the Hadamard product.

When motion correction is applied, the affine matrix is applied to the immediately following CEST acquisition, and the next vNav acquisitions that is performed after the long measurement delay. This means that the vNav images that are used to correct the CEST images for B_1^-- inhomogeneity have slightly different orientation depending on the magnitude of head movement during the previous delay as their motion correction is lacking behind. As long as subject head movement is not too large during one coregistration step, this is not a major problem since the sensitivity maps are both interpolated and heavily smoothed. In case of larger singular movement, vNav is reacquired before CEST acquisition. These reacquired vNav images are then used for adjusting the orientation of the subsequent CEST acquisition as well as B_1^-- correction of those CEST images. This ensures that the difference in image orientation between the CEST and the vNav images is minimal, although existent.

2.4 CEST sequence design

The basic structure of CEST sequence is a saturation train followed by a GRE readout. This is repeated multiple times varying the saturation frequency for each measurement. Between each measurement there is a long measurement delay, usually multiple seconds long. The saturation train may be a long continuous wave pulse, but in clinical scanners this is often not possible. Therefore a train of Gaussian pulses is used. The length, duty-cycle and amplitude of these pulses can be optimised for different metabolites.

In this study, an EPI based navigator sequence was performed interleaved with the CEST sequence. The navigators were used for real-time motion correction and retrospective receiver sensitivity correction. The navigator was placed just before the saturation train after the measurement delay. In order to accommodate possible navigator reacquisition, a small delay was placed between the navigator and the saturation train (Figure 11). The saturation module consisted of a Gaussian pulse followed by a spoiler gradient during

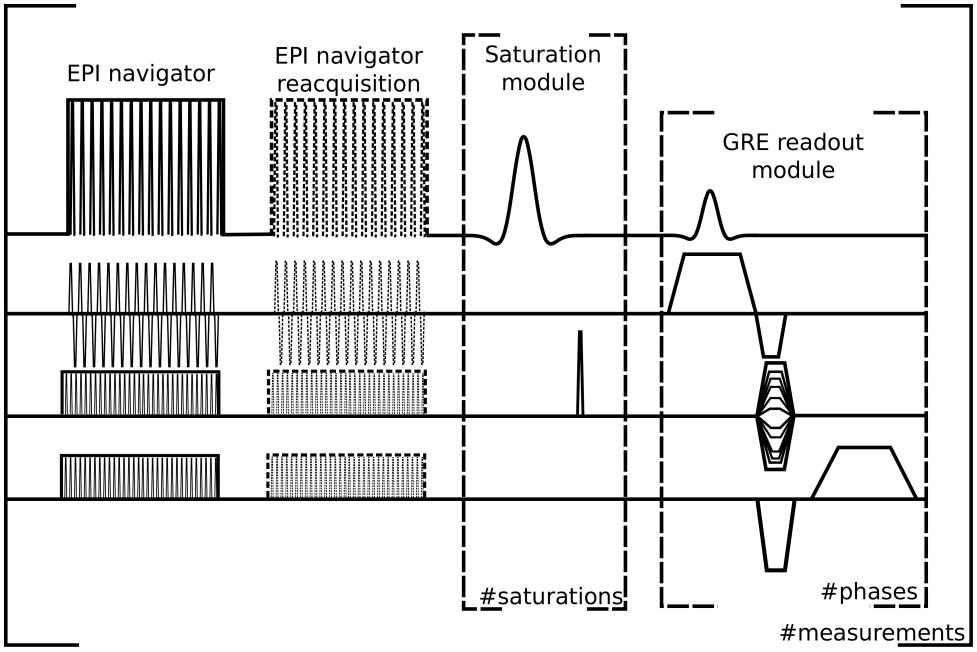

Figure 11: CEST pulse sequence diagram. The sequence consists of an echo planar imaging (EPI) based navigator sequence, a saturation module that can be repeated a set number of times, and a gradient echo (GRE) readout module that is repeated for each phase encoding step. The navigator sequence is used for real-time motion correction and subsequent retrospective receiver sensitivity correction. If the motion correction algorithm detects head motion that is larger than some predefined movement limit, the navigator sequence is immediately repeated. This ensures the adequacy of the motion correction. If the navigator is not repeated, there will be be a short delay between the EPI navigator and the beginning of the saturation module. The saturation module consists of a saturation pulse and a spoiler gradient to suppress concomitant transverse magnetisation. The direction the the spoiler gradient may be changed for each saturation pulse. The diagram is not to scale.

the interpulse delay to dephase concomitant transverse magnetisation. The polarity of the spoiler gradient was altered for each saturation pulse in the saturation pulse train. After the saturation pulse train, two consecutive GRE readouts were performed with centric k-space reordering. Both TR and TE were kept minimal to minimise relaxation before readout. Centric readout was chosen for the same reason.

Table 1: Glutamate concentrations and pH of the glutamate phantom. The phantom consisted of six vials of different glutamate solutions submerged into a cylindrical container. The container was filled with physiological solution until full.

Concentration, c (±0.1) mM	pH (±0.01)
22.4	7.05
18.0	7.05
14.1	7.04
10.4	7.04
6.1	7.04
2.1	7.04
0.0	7.06

3 Materials and methods

3.1 Glutamate phantom

Glutamate phantom was prepared into a one litre cylindrical container. The phantom consisted of seven 100 ml vials of solution with different concentrations of glutamate (L-Glutamic acid, Sigma-Aldrich, Steinheim, Germany) submerged into physiological solution within the container. The vials were prepared with 50 mM phosphate-buffered saline (PBS) solution at pH of 7.06. Due to the high acidity of glutamic acid, the final pH of the vials was adjusted to 7.05 ± 0.01 by adding 1 M sodium hydroxide (NaOH) solution until the desired pH was reached. The concentrations ranged from zero to 22.4 mM (Table 1). The vials were arranged into a hexagonal pattern so that the central vial had only buffer solution (Figure 12). Magnetic and electric properties of the phantom were not controlled. In order to discriminate the vials from each other, two straws were attached to the side of the vial with highest glutamate concentration and one straw was attached to the vial with third highest glutamate concentration (i.e. 14.1 mM).

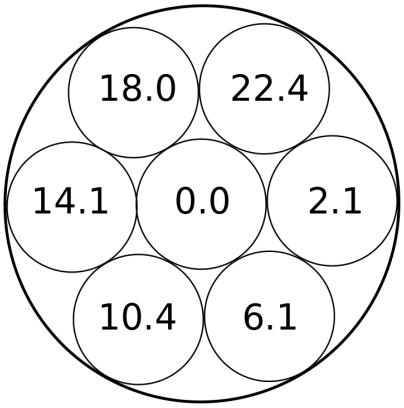

Figure 12: A cross sectional sketch of the glutamate phantom in transverse plane. The phantom consisted of a cylindrical container with six vials of differing concentrations of glutamate in phosphate-buffered saline (PBS) solution and one reference vial containing only PBS. The vials were submerged into saline solution. The numbers within the vials represents the concentration of glutamate in mM. The pH of the glutamate solutions were adjusted to 7.05 ± 0.01 by adding 1 M sodium hydroxide solution. The pH of the surrounding saline was not controlled.

3.2 Healthy volunteers

Seven healthy volunteers (4 males, 3 females; median age 31, range 21-37 years) were measured. All but one volunteer were measured several times (2 to 4 times) over a period of two months. Motion correction experiments were performed with 4 volunteers where the subjects were imaged without voluntary movement, and with up-down and left-right head movements. All experiments were performed with and without motion correction (total of six scans). Three volunteers were measured without voluntary movements to assess motion corrected CEST sequence reproducibility. These measurements were performed as a dynamic CEST experiment.

3.3 MRI protocol

All imaging sequences were performed at 7 T (Magnetom, Siemens Healthcare, Erlangen, Germany) with a 32-channel receiver head coil with combined volume coil for transmission (Nova Medical, Wilmington, MA, USA). The imaging protocol and workflow were as

follows:

1. Localiser sequence
2. AutoAlign sequence
3. Slice and shimming volume selection
4. Automatic shimming
5. Flip angle mapping sequence
6. Adjusting transmitter voltage according to flip angle map
7. vNav Setter sequence
8. Dual-echo CEST sequence

The vendor provided AutoAlign sequence was performed in order to maintain the same slice position between sessions. This was done only when the reproducibility of the CEST sequence was studied *in vivo* and not in sessions that studied motion correction.

In all *in vivo* experiments, an axial slice was selected just above the lateral ventricles. The slice was angled in the coronal plane so that it was perpendicular to the line of the third ventricle and the brain stem. The same slice, slice thickness, field of view and thus voxel size were selected for the flip angle mapping sequence and the CEST sequence. While not strictly necessary as long as both images cover the same volume, it did remove one interpolation step in post-processing thus decreasing the number of error sources. The slab of the vNav sequence was also oriented parallel to the CEST slice for the same reason. The shimming volume was set so that it covered the brain volume of the slice. Shimming was performed with vendor provided automatic shimming tool.

Turbo-FLASH -based flip angle mapping sequence was used to check B_1^+-homogeneity before CEST measurements. Due to the high exchange rate of amine protons, the saturation amplitude had to be high enough for the CEST effect to be visible. Therefore steps 5. and 6. were repeated a few times in order to make sure that the B_1^+ was not too low anywhere in the slice. The sequence parameters *in vivo* were: matrix size: 128 × 128, FOV: 256 × 256, voxel size: 2 × 2 × 8 mm^3, TR/TE: 5000/2.13 ms, number of averages: 1, pixel bandwidth: 449 Hz/px. In phantom FOV was 160 × 160 and voxel size 1.25 × 1.25 × 8 mm^3. Otherwise the parameters were the same *in vivo* and in phantom.

Although the navigator sequence was interleaved with the CEST sequence, and thus was part of the CEST sequence, it had to be set independently with a separate Setter

Table 2: Saturation frequency offsets used in the CEST experiments. Each offset is relative to the water chemical shift.

Measurement number	Offset, ppm	Measurement number	Offset, ppm
1	−4.00	14	2.60
2	−3.60	15	2.70
3	−3.40	16	2.80
4	−3.30	17	2.90
5	−3.20	18	2.95
6	−3.10	19	3.00
7	−3.05	20	3.05
8	−3.00	21	3.10
9	−2.95	22	3.20
10	−2.90	23	3.30
11	−2.80	24	3.40
12	−2.70	25	3.60
13	−2.60	26	4.00

sequence. The image volume of navigator images was chosen so that it included the whole brain volume plus at least one empty slice above the head. The slices were oriented to match the CEST slice, i.e. they had the same plane and inclination. The number of slices was normally 20. Other vNav sequence parameters *in vivo* were: matrix size: 32 × 32, FOV: 256 × 256, voxel size: 8 × 8 × 8 mm^3, EPI TR: 10 ms, TE: 3.7 ms, number of averages: 1, pixel bandwidth: 1056 Hz/px.

At the beginning of the CEST sequence there were two preparation scans to reach a steady state of magnetisation. These were followed by 27 measurements that each had a different saturation frequency from ±4.0 ppm to ±2.6 ppm relative to water chemical shift (Table 2). The central frequencies, i.e. the frequencies at or near water saturation frequency, were not measured in order to decrease total acquisition time and avoid drastic drops in image intensity of the consecutive vNav images. Higher spectral resolution (0.05 ppm) was recorded around the frequency of interest (±3 ppm). This was observed to

slightly increase MTR-asymmetry SNR, which was calculated as a moving average over ±0.2 ppm. The first measurement after the preparation scans had a saturation pulse amplitude of zero. This measurement was used as M_0 image for normalisation. In dynamic experiment, the same CEST experiment was repeated back-to-back four times within one scan. The first experiment however had consistently different contrast compared to the rest and was therefore excluded from further evaluation. The parameters of the CEST sequence were as follows if not otherwise stated; FOV: 256 × 256 mm^2, matrix size: 128 × 128, voxel size: 2 × 2 × 8 mm^3, GRE acquisition TR: 7 ms, TE: 2.04/4.08 ms, flip angle 5°, receiver bandwidth: 950 Hz/px, measurement TR: 8600 ms, number of measurements: 27. The saturation sequence consisted of three 100 ms Gaussian pulses with 12 ms interpulse delay and B_{1rms} of 3.04 μT.

The navigator reacquisition threshold was set to ≥0.4 mm or ≥0.4°. If the navigator detected head motion exceeding either of these values in one coregistration step, reacquisition would fire. These values were chosen based on previous MRS experiments [30].

3.4 Data processing

All data processing was performed on in-house built MATLAB scripts (R2017a, Natick, MA, USA). The post processing image pipeline was the following:

1. Calculate ΔB_0-maps from the CEST phase images
2. Calculate sensitivity maps from the vNav images
3. Apply sensitivity correction (B_1^--correction) to the CEST images
4. Normalise the CEST images by the M_0 image
5. Apply B_0-correction to the CEST images
6. Interpolate B_1^+-corrected CEST images
7. Calculate MTR-asymmetry maps from the corrected CEST images

The images were collected combined and uncombined. The uncombined magnitude images were not used, and were thus discarded. For each CEST offset there were two combined magnitude images, one for each echo. These were combined into a series of

CEST offset images by

$$Z(\Delta\omega) = \frac{1}{k}\sum_{e=1}^{k}\frac{M_e(\Delta\omega)}{M_{0,e}} \tag{24}$$

where $Z(\Delta\omega)$ is the normalised CEST image matrix as a function of offset, k is the total number of echos, and e is the echo number. $M_e(\Delta\omega)$ and $M_{0,e}$ are the unnormalised CEST images as a function of offset and the unsaturated CEST image respectively.

The combination of the uncombined phase CEST images and the subsequent phase difference maps were calculated by using voxel-by-voxel Hermitian inner product [54]:

$$\Theta_e(\Delta\omega) = \angle\sum_{l}\left(M_{1l}(\Delta\omega)\circ M_{2l}(\Delta\omega)\circ e^{i(\theta_{2l}(\Delta\omega)-\theta_{1l}(\Delta\omega))}\right). \tag{25}$$

The operator $\angle$ denotes the four-quadrant tangent inverse of the complex sum. $M_{1l}(\Delta\omega)$ and $M_{2l}(\Delta\omega)$ denote the unnormalised CEST images of channel l for echos one and two respectively. Similarly $\theta_{1l}(\Delta\omega)$ and $\theta_{2l}(\Delta\omega)$ are the uncombined CEST phase images of the two echoes for each channel l. Operator $\circ$ denotes the Hadamard product.

The principle behind ΔB_0-correction was described in Section 2.3.1. The dynamic ΔB_0-correction was applied by shifting the data points of the Z-spectrum in x-axis relative to each other, i.e. assigning new ppm value to each pixel in each CEST image. Then new data points were interpolated for the old ppm values to preserve the offset distribution and enable asymmetry analysis. This interpolation was done by using MATLAB's implementation of piecewise cubic Hermite interpolating polynomial (pchip). However, before the images were ΔB_0-corrected, B_1^--correction was applied. The reasoning behind this was that the sensitivity maps were time dependent rather than offset dependent and scaled the images based on their intensity values. ΔB_0-correction changed the intensity values thus changing the magnitude of correction.

B_1^+-correction, on the other hand, is not dependent on the offset value or time. It is rather done based on the Z-value, B_1-map and nominal saturation amplitude. The theory behind this is explained in Section 2.3.2. The B_1^+-correction is incidentally applied after B_1^-- and ΔB_0-corrections.

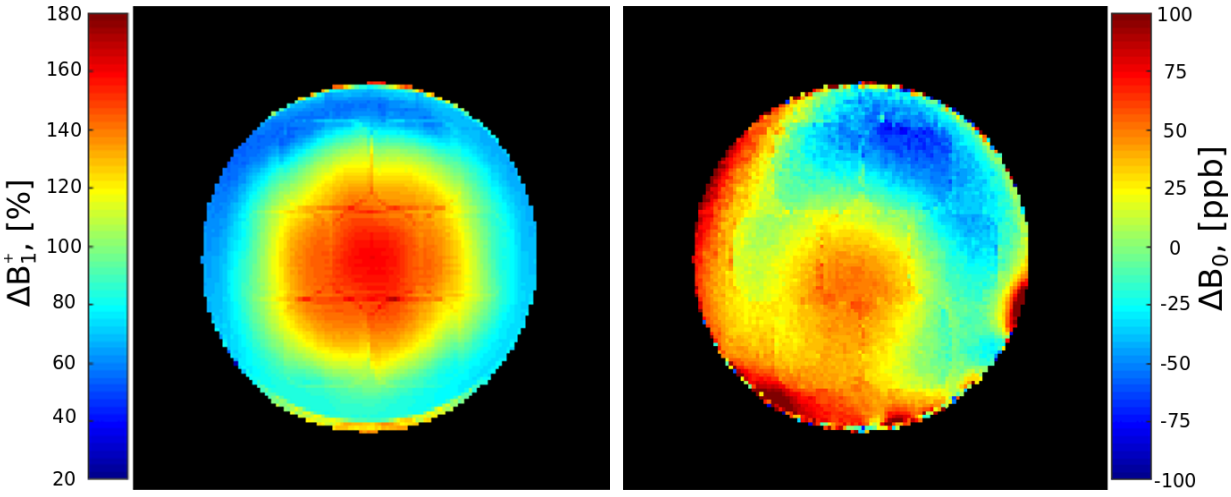

(a) (b)

Figure 13: Maps showing the relative and absolute changes in B_1^+ (a) and B_0 (b) respectively in phantom. The B_1^+-map is calculated from a flip angle map measured before the CEST sequence. The flip angle map was normalised to 100 % which corresponds to a 90 degree pulse. The B_0-map is calculated from phase difference CEST maps. This particular map corresponds to the second measurement in one CEST experiment. The change in the B_0-field in represented in parts-per-billion (ppb).

4 Results

4.1 Phantom results

Both B_1^+- and B_0-inhomogeneities were detected in phantom (Figure 13). The B_1^+-field was very low (∼60% of nominal flip angle) around the edge of the phantom and very high (∼160%) in the centre. On the other hand, B_0 was rather homogeneous in the phantom, only -0.5 ± 40 ppb. In the CEST images, regions of hypointensity were observed in the peripheral areas of the phantom whereas the centre vial was consistently hyperintense. The standard deviation of image intensity within a vial could be as high as 25%. These intensity inhomogeneities corresponded to flip angle inhomogeneities in the flip angle maps (Figure 13) rather than B_0 maps and were thus attributed to be B_1^+-inhomogeneities. These B_1^+-inhomogeneities could also be detected in the MTR-asymmetry maps but only in vials that contained glutamate (Figure 14). Applying B_1^+-correction significantly improved MTR-asymmetry map quality as can be seen in figure 15.

Phantom images exhibited consistently low MTR-asymmetry SNR throughout the experiments (Figure 14). This was solved by measuring phantom experiments as dynamic

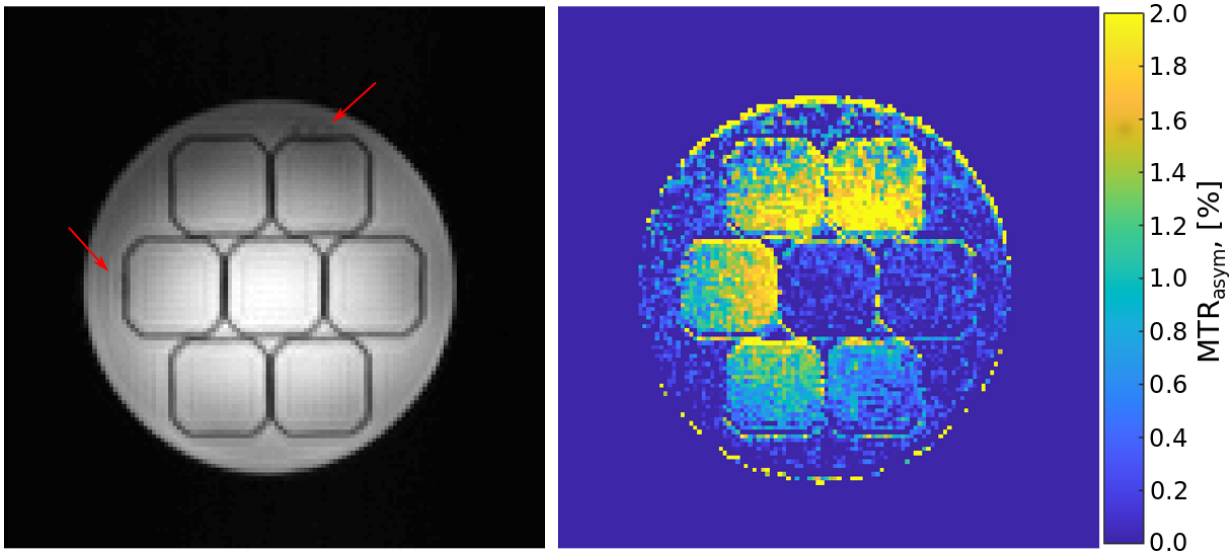

(a) (b)

Figure 14: A CEST image (a) at 3.3 ppm from water. The red arrows point to the straws that designate what glutamate concentrations the vials have and in what order. The upper arrow points to the two straws which are attached to the vial with highest glutamate concentration and the leftmost arrow points to the single straw attached to vial with third highest glutamate concentration. MTR-asymmetry map (b) at 3.0 ppm from water shows an increase in contrast that closely match the glutamate concentration. The saturation pulse amplitude was 4.5 μT.

CEST experiments. As there were no temporal glutamate changes within the phantom during these dynamic measurement, these repetitions were used to average the MTR-asymmetry maps for better quality and higher SNR (Figure 15). The dynamic experiment consisted of four repetitions, however, due to the difference in contrast, the first repetition was excluded. Therefore all phantom MTR-asymmetry maps were an average of three maps.

MTR-asymmetry showed a significant linear correlation (Pearson's r = 0.986, $p < 10^{-4}$) with glutamate concentration (Figure 16.) when B_1^+-inhomogeneity correction was not applied. Applying B_1^+-inhomogeneity correction improved image quality and changed standard deviation of MTR-asymmetry within a glutamate vial by a factor of 0.5 $\pm$ 0.1 (Figure 15) therefore making the contrast within a vial more homogeneous. This also slightly improved correlation between the MTR-asymmetry and glutamate concentration (Pearson's r = 0.995, $p < 10^{-5}$). The difference in the MTR-asymmetry between the vial with the lowest glutamate concentration (vial no. 2, 2.1 mM) and the vial without any glutamate was significant ($p < 10^{-8}$). Similarly, the difference in the MTR-asymmetry

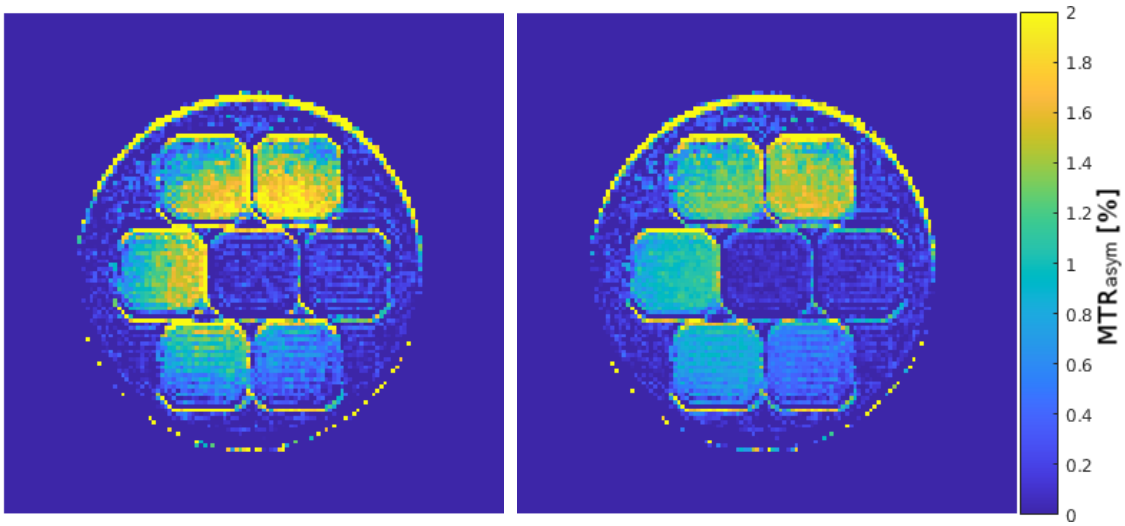

(a) (b)

Figure 15: Example images of MTR asymmetry maps of the glutamate phantom at 3.0 ppm from water. Each vial has a different glutamate concentration, highest concentration being in the rightmost vial of the top row. The concentration decreases linearly in counter clockwise direction. Before the maps were calculated, the Z-spectra were B_0 corrected by using dual-echo gradient echo CEST approach [47]. After this B_1^+ correction is applied. Maps (a) and (b) show the effect of B_1^+-inhomogeneity. In map (a), the B_1^+-inhomogeneity has not been corrected. This manifests as hyperintensity near the centre of the phantom and hypointensity in the peripheries. Applying B_1^+-inhomogeneity correction decreases the effect to some degree. Two measurements with two different saturation pulse amplitude were used for the B_1^+ correction. The saturation pulse amplitudes were 4.2 μT and 4.5 μT and the resultant images were corrected to 4.2 μT. The field of view was 160 $\times$ 160 mm^2, voxel size 1.25 $\times$ 1.25 $\times$ 5.0 mm^3, number of averages 3, and pixel bandwidth 1563 Hz/px. The rest of the imaging parameters were as described in Section 3.3.

between the vial number 2 and the volume outside of the vials but inside the phantom was significant ($p < 10^{-4}$). However, these differences were small compared to vials with higher concentration of glutamate and thus steep windowing was necessary for the difference to be apparent visually.

A non-zero, positive baseline MTR-asymmetry was consistently detected in zero-glutamate vials as well as outside the vials in all phantom experiments. The magnitude of this baseline was dependent on the CEST imaging parameters.

Correlation between glutamate concentration and MTR-asymmetry could also be detected in saturation offsets other than 3 ppm. However, due to the distribution of

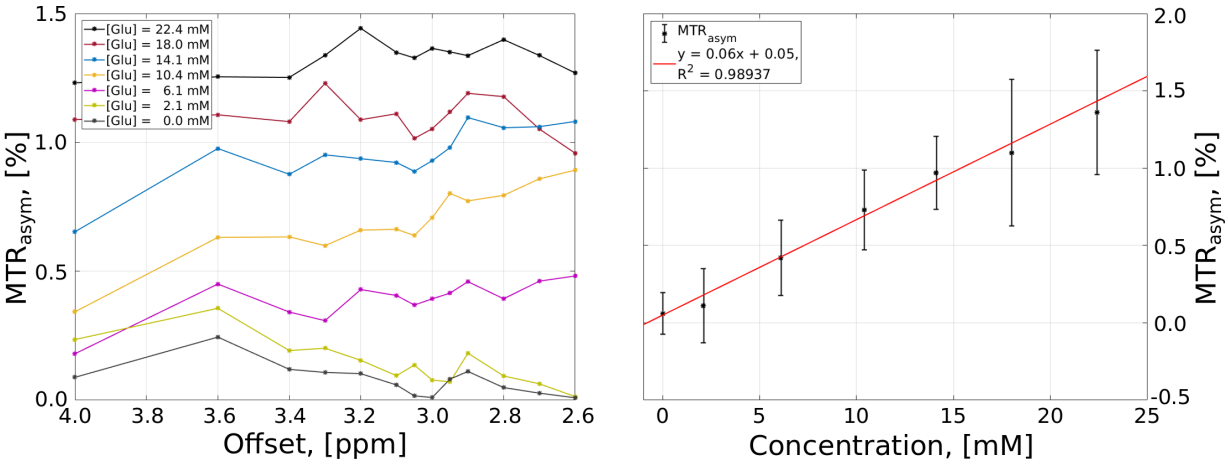

(a) (b)

Figure 16: MTR asymmetry as a function of saturation offset (a). The different lines represent different phantom glutamate concentrations. Mean MTR asymmetry at 3.0 ± 0.2 ppm as a function of glutamate concentration (b). The bars represent one standard deviation. The CEST images were B_0 an B_1^+ corrected before analysis.

measured offset values concentrating around 3.0 ppm, the extent of this correlation was not studied.

4.2 Volunteer results

Strong B_1^+-inhomogeneities were also detected *in vivo*, as is evident from the B_1^+-map in Figure 18. Especially in the right cortical region as well as in the middle of the brain and to lesser extent in the left cortical region. B_0-inhomogeneities were also detected. The B_1^+-inhomogeneities were observed to be smaller *in vivo* than in phantom, whereas B_0-inhomogeneities were larger *in vivo* compared to phantom.

Higher MTR-asymmetry values were consistently observed in grey matter compared to white matter. This may be attributed to difference in white matter/grey matter glutamate concentrations [11]. When motion correction was not applied, motion artifacts due to involuntary head movement were occasionally observed. Enabling the real-time motion correction noticeably improved the image quality in case of involuntary head movement (Figure 19) and decreased the number of maps with motion artifacts from 18 % of cases down to 0 % (4/22 maps versus 0/18 maps). The length of the measurement likely affected the probability of involuntary head movement.

Voluntary head movement produced severe motion artifacts regardless of motion

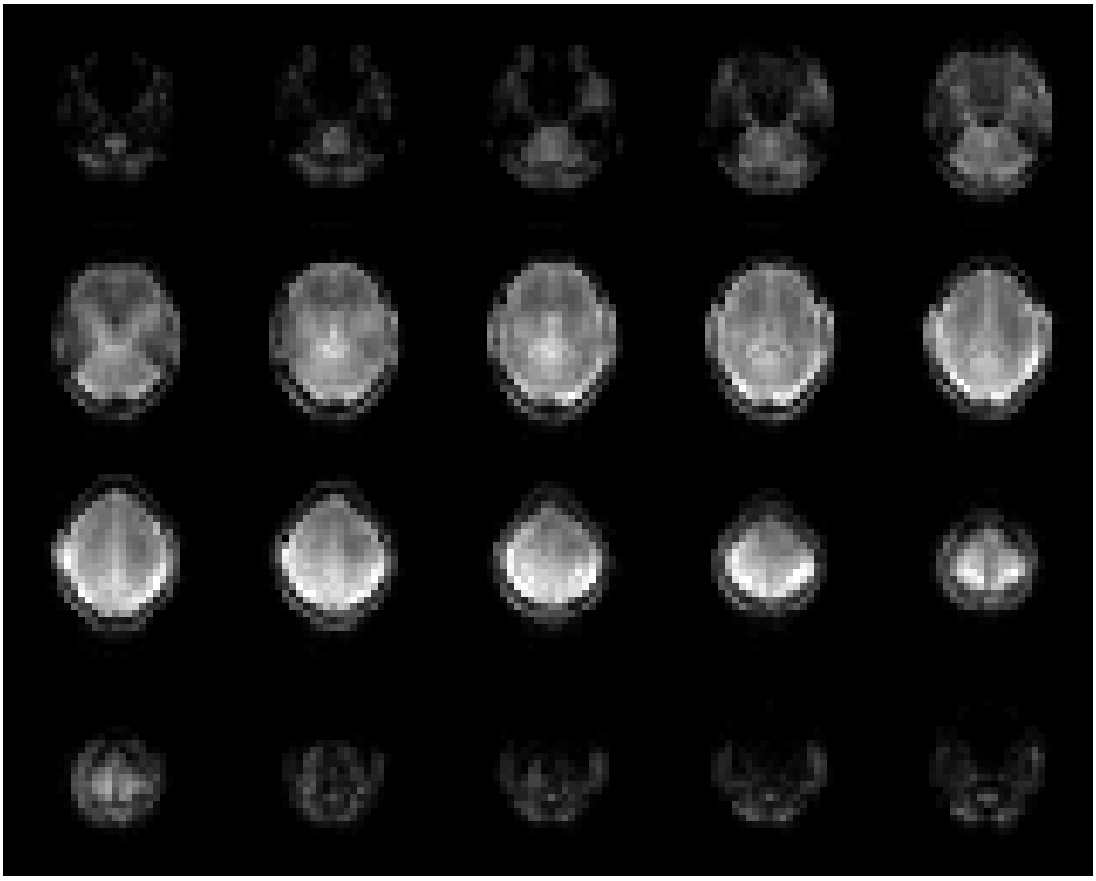

Figure 17: Mosaic representation of volumetric echo-planar imaging (EPI) navigator images. The last four images on the bottom row are folding artifacts and should be empty. This does not affect motion correction algorithm. The imaging parameters were: matrix size: 32 × 32, number of slabs: 20, FOV: 256 × 256, voxel size: 8 × 8 × 8 mm^3, EPI TR: 10 ms, TE: 3.7 ms, number of averages: 1, pixel bandwidth: 1056 Hz/px

correction. Although enabling motion correction greatly alleviated motion artifacts, complete artifact removal could not be achieved in case of large singular movement (>0.7 ° in one coregistration step) even with reacquisition (Figure 20). An actual threshold head motion that the motion correction was able to correct could not be accurately determined due to difficulty to reproduce head movements and consistently produce small enough motion. The direction of voluntary head movement was not found to affect the quality or efficacy of motion correction.

On average, involuntary head movement was found to induce B_1^--inhomogeneities ranging 0.2 ± 0.5 % over the course of one CEST experiment (∼4.5 min), i.e. the receiver sensitivity fluctuated this much during one experiment. The effect this had on MTR-asymmetry depended on when the movement occurred and which direction offsets were

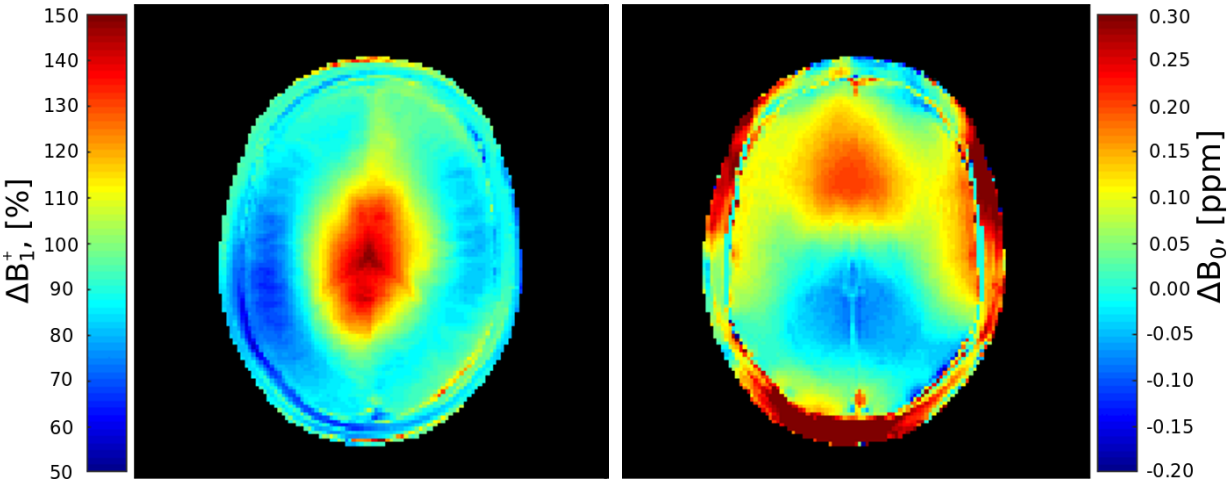

(a) (b)

Figure 18: Maps showing the relative and the absolute changes in B_1^+ (a) and B_0 (b) respectively *in vivo*. The B_1^+-map is calculated from an flip angle map measured before the CEST sequence. The flip angle map was normalised to 100 % which corresponds to 90 degree pulse. Notice the extensive hyposaturation in the right cortical region. The B_0-map was calculated from the phase difference CEST maps. This map corresponds to the second measurement in one CEST experiment. The change in the B_0-field is represented in ppm.

measured. Performing B_1^--correction changed the MTR-asymmetry by 4 ± 100 % (e.g. $MTR_{mathrmasym}$ changed from 1.2 % to 2.0 % in the frontal lobe white matter). These changes were not always visually obvious in MTR-asymmetry maps, however they could affect further MTR-analysis.

The effects of B_1^--corrections were more obvious when the subject performed relatively large (>1 °) head rotation during the measurement (Figure 21). When the subject was asked to turn their head to left from neutral position, B_1^- decreased by -2.0 ± 0.3 % in the right hemisphere and increased by 0.4 ± 0.2 % in the left hemisphere (Figure 22). A decrease in B_1^- could be observed in both hemispheres before voluntary movement began. Similar decrease was observed in all subjects. If the change in B_1^- after movement is compared to this lower baseline, these B_1^- changes were -1.4 ± 0.3 % and 0.9 ± 0.2 % for right and left hemispheres respectively.

Performing B_1^--correction in the case of voluntary head motion resulted in more homogeneous MTR-asymmetry distribution bilaterally. The ratios between MTR-asymmetry values in the right and the left hemispheres were 0.6 ± 0.4, 2.0 ± 1.3, and 0.9 ± 1.2 when subject did not move, when subject was asked to move but B_1^- was not corrected, and

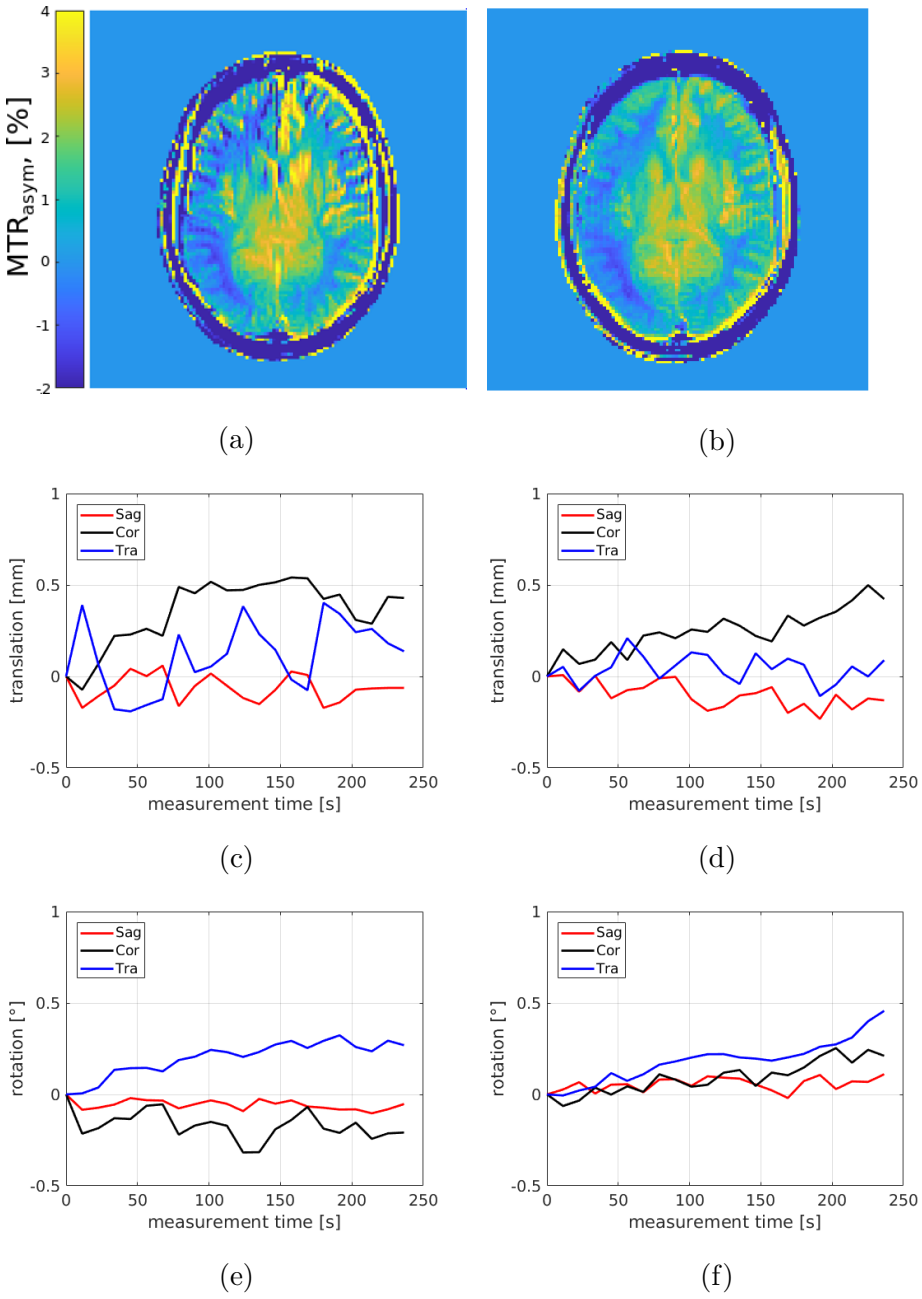

Figure 19: A volunteer CEST measurement where the subject was asked not to move during the measurement. The measurement was repeated without (a, c, and e) and with (b, d, and f) motion correction. EPI navigator sequence was enabled in both cases and subject head movement was recorded. Graphs c, d, e, and f show the translation (c and d) and rotation (d and f) of the subject's head in three different planes. In both experiments the subjects involuntary head movement was of the same order, however the first experiment produced noticeably worse images (a) when compared to motion corrected experiment (b). Both images were B_0 and B_1^+ corrected. The imaging parameters are listed in Section 3.3. The measurement time for one CEST experiment was ~4.30 min.

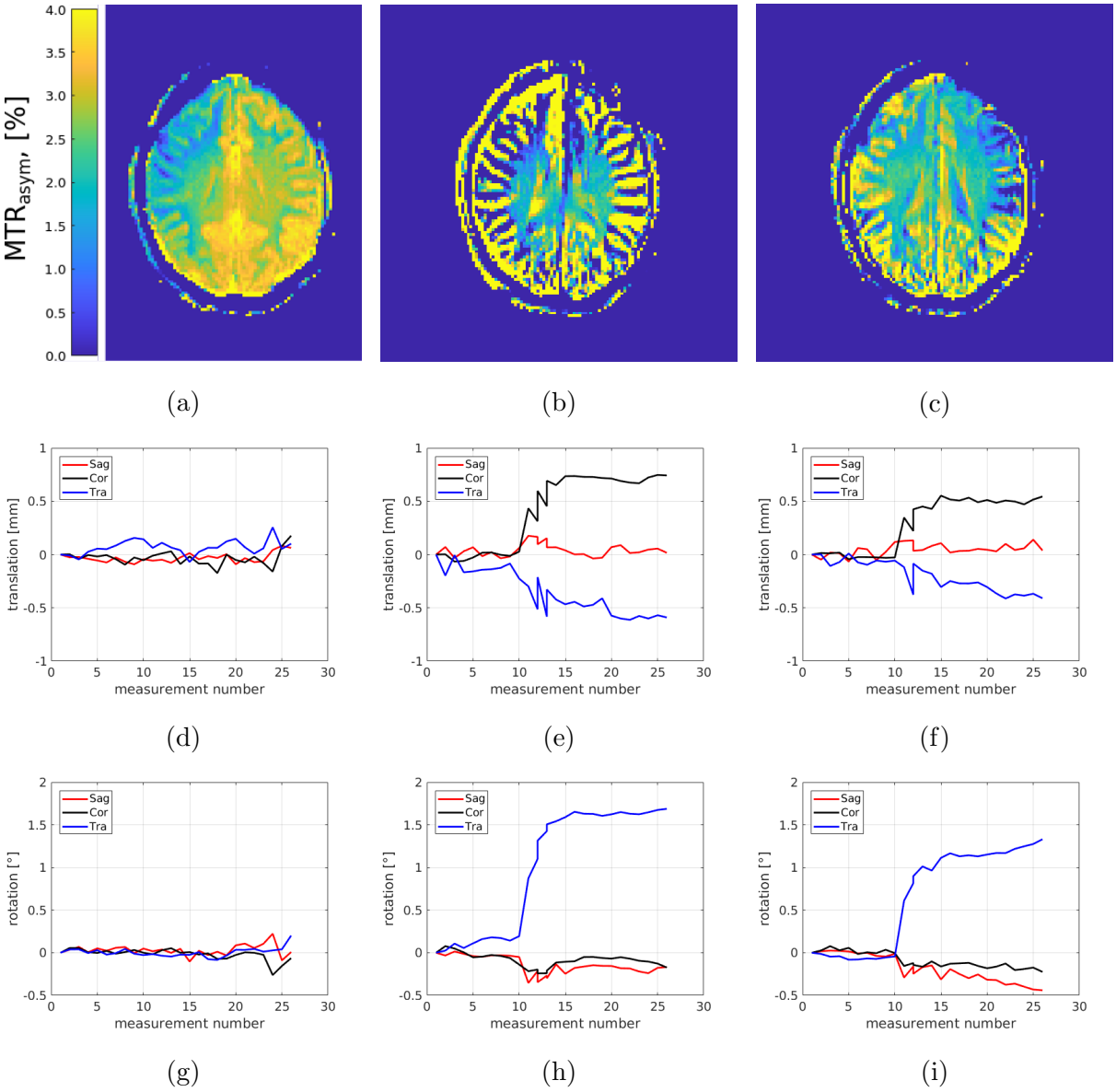

Figure 20: MTR asymmetry maps showing the effect of large movement during the measurement. First experiment was performed with motion correction on and the subject was asked not to move (a). The experiment was then repeated without motion correction, but after the ninth measured offset the subject was asked to gradually rotate their head from right to left over a period of three offset measurements (b). This was repeated with the motion correction on (c). Each movement was performed during the delay between two consecutive offset measurements. Graphs d through i show the corresponding subject head translation (d, e, and f) and rotation (g, h, and i) in sagittal (Sag), coronal (Cor), and transverse (Tra) planes for each experiments. Navigator reacquisition was triggered at 12th and 13th measurements during the second experiment (b, e, h) and at 12th measurement during the third experiment (c, f, i). All CEST images were B_0 and B_1^+ corrected but not B_1^- corrected. B_{1rms} of 3.8 μT was used.

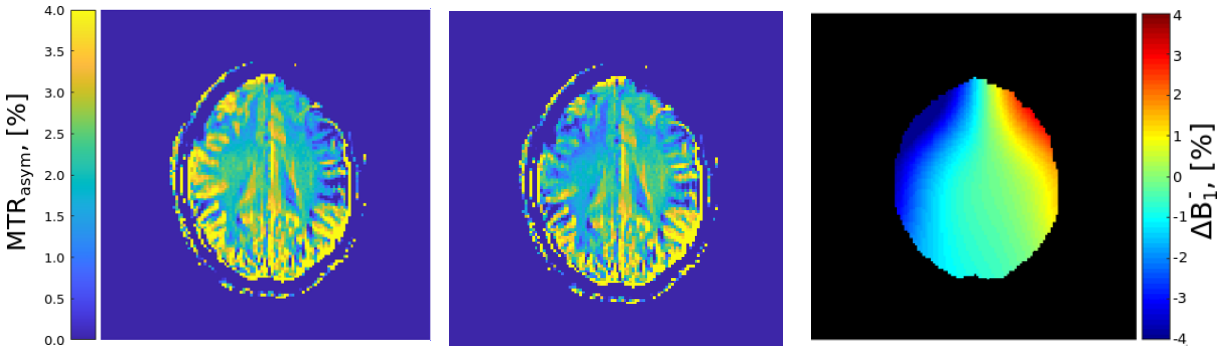

(a) (b) (c)

Figure 21: The subject was asked to rotate their head from right to left during the measurement. Depending on which direction offsets are measurement (from for example -4 to 4 ppm or 4 to -4 ppm.), this motion induces MTR asymmetry hyperintensity on the other side of the brain and hypointensity on the other (a) due to the patient moving closer to receiver coil elements on the left side. This change in sensitivity is clearly visible in ΔB_1^- map (c) which corresponds to offset measurement 12. The intensity of each raw CEST image was changed proportionally according to the ΔB_1^- maps. This results in a corrected MTR asymmetry map (b). B_0 and B_1^+ corrections were applied after the B_1^- correction.

when subject was asked to move and B_1^- was corrected respectively. B_1^--correction was found to make the Z-spectra more symmetrical around water (Figure 23).

In dynamic experiments a fluctuation of MTR-asymmetry was observed. The difference in MTR-asymmetry values between repetitions was not significant ($p > 0.5$). MTR-asymmetry maps fluctuated on average 4 % over the repetitions (mean standard deviation of MTR-asymmetry value of each voxel: 4 ± 2 % over three repeated CEST experiments over the whole slice). The change in MTR-asymmetry was 4 ± 2% in the cortical grey matter and 3 ± 1 % in white matter between three repetitions (Figure 24). Similar results were observed in equivalent phantom experiment (7 ± 3 % over all vials, no significant difference between repetitions).

Comparing MTR-asymmetry values of one subject showed significant change in MTR-asymmetry of 10 % in white matter (2.2 ± 0.2 versus 2.0 ± 0.2, $p < 10^{-32}$) and 13 % in grey matter (2.3 ± 0.5 versus 2.0 ± 0.8, $p < 10^{-13}$) between two scans performed 1.5 weeks apart.

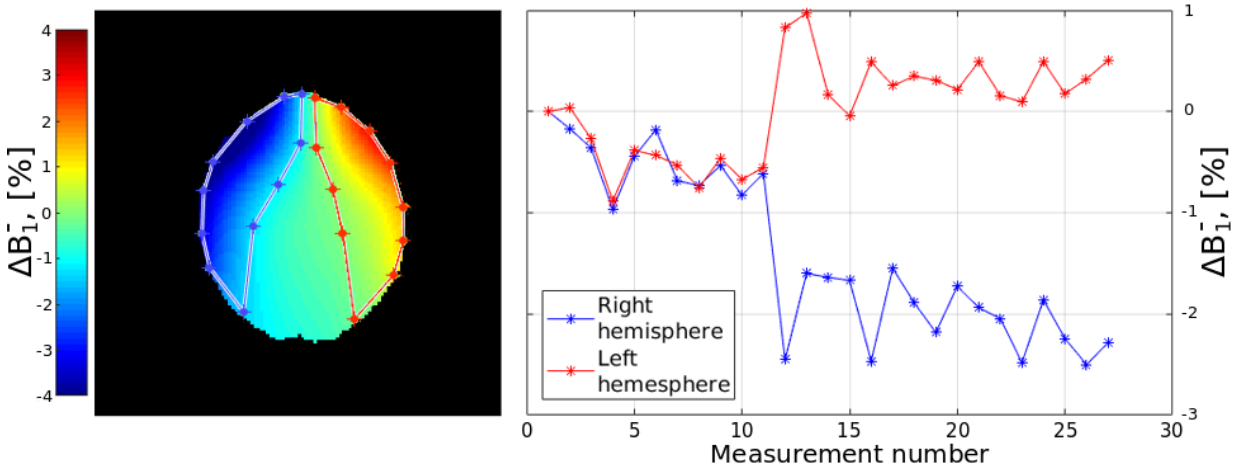

(a) (b)

Figure 22: The subject was asked to rotate their head from right to left after the ninth offset measurement. This results in left hemisphere nearing to, and the right hemisphere furthering from the receiver coils. This change in receiver sensitivity may be quantified by calculating the change in EPI navigator image intensities with respect to the first navigator images, and normalising the difference by the first images. The sensitivity change map (a) corresponds to twelfth offset measurement. A region of interest was drawn on both sides of the brain and the mean sensitivity change was plotted as a function of measurement numbers (b). Note the bilateral decrease in receiver sensitivity during the first 10 measurements. B_{1rms} of 3.8 μT was used.

5 Discussion

5.1 Phantom

MTR-asymmetry was observed to exhibit a significant linear dependency on glutamate concentration in the phantom (Figure 16) at 3 ppm from water. This is in agreement with previously published results [11]. The gradient of the linear fit strongly depends on the used experimental parameters, such as saturation amplitude, and system parameters, such as T_1, and thus cannot be used to determine concentration directly as such without more extensive analysis. This, however, shows that the MTR-asymmetry is sensitive to glutamate and can be used as an indicator for glutamate concentration.

In phantom, the lowest resolvable glutamate concentration from background was 2.1 $\pm$ 0.1 mM. This was, however, only barely resolvable and only after three averages. In general, the phantom suffered from low SNR and poor B_1^+-homogeneity. The low SNR

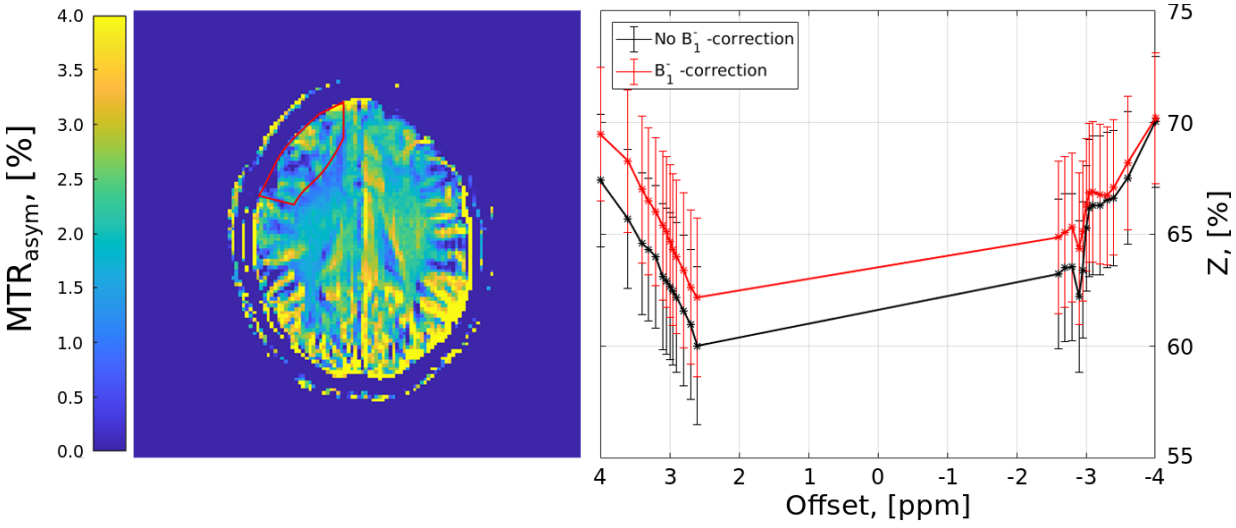

(a) (b)

Figure 23: Correcting the CEST images for B_1^--inhomogeneity improved Z-spectra by making them more symmetrical around water for offsets further away from water where no amine exchange should occur (>4 ppm). The black line shows Z-spectra before B_1^--correction and the red line after B_1^--correction. Data is from the ROI shown in red on map (a). The subject was asked to rotate their head from right to left after the ninth offset measurement.

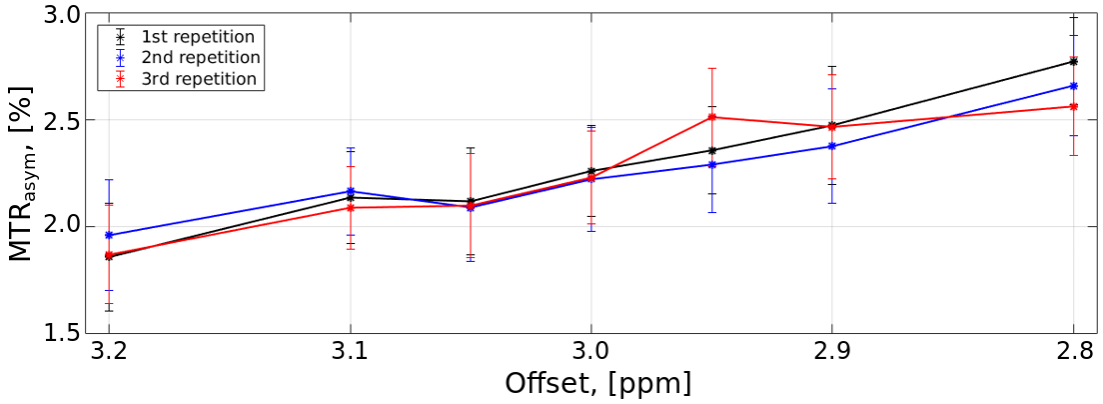

Figure 24: An example figure of white matter MTR-asymmetry as a function of offset for three identical CEST experiments performed back-to-back within one scan. The fluctuation of MTR-asymmetry was approximately 2 % within a region of interest over the three repetitions.

was not observed *in vivo*. Neither relaxation times nor electric properties of the phantom were controlled and this might have adversely affected the SNR. Therefore, it could not be conclusively determined whether 2.1 ± 0.1 mM difference in glutamate concentration is resolvable *in vivo*.

The pH of the phantom was controlled with a phosphate-buffered saline solution and fine tuned with sodium hydroxide solution to match the desired pH. This was done

to control the glutamate amine exchange rate. It was not, however, considered that the HPO_4^{2-} also catalyses proton exchange and thus also affects the exchange rate [55]. The pH and the buffer concentrations were kept constant for all glutamate vials and thus there should not be exchange rate differences between the vials. This buffer effect should be kept in mind for future experiments, especially if pH quantification is sought after.

Although the pH of the glutamate vials were controlled, the temperature of the phantom was not. Temperature affects the rate of chemical reactions and thus also the rate of exchange (Equation 13). GluCEST experiments at 23 °C have been shown to have twice the MTR-asymmetry contrast compared to identical experiments performed at 37 °C [55]. This further complicates quantitative evaluation of phantom results. However, as the phantom was merely used to confirm the visibility of glutamate and concentration sensitivity of CEST-MRI, the temperature of the phantom was not considered to be of great importance.

In order to better assess the efficacy of CEST-MRI and related correction methods, a phantom more closely resembling human brain in terms of relaxation times and electric properties should be used. If a glutamate phantom is to be used for optimising sequence parameters, a water bath or some other means should be used to compensate for differing exchange rates in phantom and *in vivo*. Additionally, an array of vials with finer differences in glutamate concentrations would be required to assess the concentration resolution of CEST-MRI.

5.2 Volunteers

Higher MTR-asymmetry values were observed in grey matter than in white matter. This is consistent with previously published results [11, 20] and may be due to difference in white matter/grey matter glutamate concentrations.

Involuntary head movement was observed to cause visible motion artifacts in the MTR-asymmetry maps (Figure 19). Applying real-time motion correction eliminated these effects completely. However, the experiments were not completely identical in terms of measurement time (dynamic experiments vs. single experiments) and the sample size was small (40 maps in total). Also, the same degree of movement was hard to reproduce due to its nature and thus only approximate comparison was possible. The correction potential of the real-time motion correction method was assessed by controlled head move-

ment experiments. As long as total motion during one coregistration step did not exceed 0.7 mm or 0.7 ° the motion correction worked well. Larger singular movement resulted in bad correction regardless of reacquisition. This is not necessarily the upper limit of successful motion correction as it is hard to replicate such a small movements *in vivo* and thus the actual limits could not be determined with such a small sample size. The direction of movement or the total movement during the period of the experiment were observed not to affect the MTR-asymmetry map quality regarding movement artifacts. This would suggest that slow, drifting motion during the experiment could be adequately corrected even if it would amount to large overall movement over the course of the whole experiment. To better assess the efficacy of real-time motion correction, a larger subject population should be measured for more robust statistical analysis to determine upper limits for successful motion correction.

Although the direction of voluntary head movement was not found to affect the quality or efficacy of motion correction, this does not mean that translation and rotation are equivalent with respect to the efficacy of the motion correction algorithm. In these experiments, reacquisition of the navigator would trigger if threshold movement limits of 0.4 mm and 0.4 ° were reached. There probably is room for optimisation in these values to further improve the motion correction.

One possible reason for rather poor motion correction performance is the lack of contrast within the brain, as is evident in Figure 17. In MRSI, due to the use of water suppression sequence, cerebrospinal fluid (CSF) appears dark giving better contrast between CSF and brain matter. This may improve motion correction algorithm. This is, however, not possible for CEST-MRI leaving room for further optimisation of the motion correction sequence as well as the algorithm to be better suited for CEST-MRI.

A clear disadvantage of this motion correction method is that it cannot correct motion that occurs during navigator acquisition, saturation, or CEST acquisition, or the short delays between these. Only motion that occurs between the long delay between two measurements is corrected. However, as this delay is very long compared to the rest of the sequence (>8 seconds vs. ∼1 second), it is reasonable to assume that most movement occurs during this delay.

Another disadvantage is that this method is sensitive to saturation effects. The contrast of the vNav images must not change appreciably during the course of the experiment or else the motion correction algorithm may apply erroneous corrections to the

CEST and the vNav gradients. The magnitude of water saturation at the starts of the vNav acquisition depends on the frequency of saturation pulses and the length of time delay between consecutive measurements. If all frequencies, including those that are close to or at water saturation frequency, are to be measured, the measurement delay must be long enough for water to relax completely. The measurement time was shortened by not acquiring offsets near water. This meant that shorter measurement delay could be used. With measurement delay of 8 seconds between the end of a CEST acquisition and the beginning of the next vNav acquisition, and closest frequency to water being ± 2.60 ppm, some bilateral signal suppression was still observed in the vNav images (Figure 22). This was not observed to affect the motion correction, however this decrease is corrected by the B_1^--correction. The effect this had on MTR-asymmetry was not studied, however it was likely negligible as the saturation reached a steady state after a few measurements. However, this effect should be kept in mind in future experiments. In principle, the measurement delay can still be nearly arbitrarily short with the vNav motion correction if the frequency of interest is far from water and the frequencies close to water are not measured. This also means that vNav motion correction might not be feasible with short measurement delays when measuring labile protons near water frequency, such as –OH protons.

The vNav images were successfully used to measure receiver coil sensitivity changes during CEST experiments. Applying dynamic B_1^--correction improved MTR-asymmetry map quality, made MTR-asymmetry bilaterally more homogeneous and improved Z-spectra symmetry far from water. During involuntary head movement the correction was rather small and not always visually apparent due to the scarcity of head movement. These changes might still be significant in quantitative CEST measurements and therefore dynamic B_1^--correction could be important correction method in future CEST experiments.

Reproducibility of CEST-MRI over a period of several weeks could not be verified. Comparison between MTR-asymmetry values showed significant changes in both white and grey matter (10 % and 13 % respectively) over the period of the study. Such large changes both in magnitude and area cannot be explained with physiological changes and are thus probably due to changes in experimental conditions. All imaging parameters were kept constant and the same slice was selected by manufacturer provided auto-align system. Shimming was performed with manufacturer provided auto-shimming system at

the beginning of each imaging session. The shimming voltages were not identical between measurements and this might be a source of fluctuation in MTR-asymmetry values.

Fluctuation in MTR-asymmetry values was also observed in dynamic CEST experiments where the same CEST experiment was repeated multiple times during one scan. However, in dynamic experiments the fluctuation was not significant ($\sim$4 % over all repetition and whole slice, $p > 0.5$). The fluctuation probably arises mostly from noise rather than physiological effects. In phantom, the fluctuation was even higher ($\sim$7 % over three repetitions) due to the lower SNR.

Dynamic experiments are probably the way forward for CEST-MRI due to its ease of implementation and interpretation. So far glucose has been successfully utilised as an exogenous contrast agent in dynamic glucose enhancement (DCE) glucoCEST experiments [14, 56, 57]. Such experiments may provide an additional diagnostic tool to complement or even partly replace fluorodeoxyglucose - positron emission tomography (^{18}FDG-PET) experiments. Research in other exogenous CEST contrast agents is ongoing. Some more experimental contrast agents, such as hyperpolarised ^{129}Xe in cryptophane-A molecular cages, have the advantages of having extremely high sensitivity (nM in Xe-HyperCEST versus mM in GluCEST) and large chemical shift from water (130 ppm for Xe-HyperCEST versus 3 ppm GluCEST).[58] Such contrast agents are yet to be used *in vivo*, but offer a great potential for future research. Dynamic CEST experiments are in general longer than singular CEST experiments. This necessitates some form of motion correction in order to minimise false interpretations. Real-time motion correction coupled with dynamic B_1^--correction as implemented in this thesis provide a potential solution to motion related artifacts.

6 Conclusion

Real-time motion correction method was successfully implemented in CEST-MRI sequence. The method was shown to be able to correct for small, involuntary head movements *in vivo*. This improved GluCEST MTR-asymmetry map quality. Larger, sudden head movements could not be accurately corrected. Additionally, a dynamic B_1^--correction method was devised. This was shown to be able to correct for motion related receiver coil sensitivity changes that may produce asymmetry in the Z-spectra that may be erroneously interpreted as proton exchange.

References

[1] P. C. Lauterbur, "Image formation by induced local interactions: Examples employing nuclear magnetic resonance," *Nature*, vol. 242, pp. 190 EP –, Mar 1973.

[2] P. Mansfield and P. K. Grannell, "NMR 'diffraction' in solids?," *Journal of Physics C: Solid State Physics*, vol. 6, no. 22, p. L422, 1973.

[3] R. D. Muchow, D. K. Resnick, M. P. Abdel, A. Munoz, and P. A. Anderson, "Magnetic resonance imaging (MRI) in the clearance of the cervical spine in blunt trauma: A meta-analysis.," *Journal of Trauma-Injury Infection & Critical Care*, vol. 64, no. 1, pp. 179–189, 2008.

[4] S. W. E. Atlas, *Magnetic Resonance Imaging of the Brain and Spine*. Lippincott Williams & Wilkins, Inc., 4 ed., 2008.

[5] I. I. Rabi, J. R. Zacharias, S. Millman, and P. Kusch, "A new method of measuring nuclear magnetic moment," *Phys. Rev.*, vol. 53, pp. 318–318, Feb 1938.

[6] K. Ward, A. Aletras, and R. Balaban, "A new class of contrast agents for MRI based on proton chemical exchange dependent saturation transfer (CEST)," *Journal of Magnetic Resonance*, vol. 143, no. 1, pp. 79 – 87, 2000.

[7] K. U. Linderstrøm-Lang, "Deuterium exchange and protein structure," in *Symposium on Protein Structure*, pp. 23–34, 1958.

[8] S. D. Wolff and R. S. Balaban, "Magnetization transfer contrast (MTC) and tissue water proton relaxation in vivo," *Magnetic Resonance in Medicine*, vol. 10, no. 1, pp. 135–144, 1989.

[9] R. M. Henkelman, G. J. Stanisz, and S. J. Graham, "Magnetization transfer in MRI: a review," *NMR in Biomedicine*, vol. 14, no. 2, pp. 57–64, 2001.

[10] M. Bernstein, K. King, and Z. Xiaohong, *Handbook of MRI Pulse Sequences*. Academic Press, 1 ed., 2004.

[11] K. Cai, M. Haris, A. Singh, F. Kogan, J. H. Greenberg, H. Hariharan, J. A. Detre, and R. Reddy, "Magnetic resonance imaging of glutamate," *Nature Medicine*, vol. 18, pp. 302 EP –, Jan 2012.

[12] P. Z. Sun, G. Xiao, I. Y. Zhou, Y. Guo, and R. Wu, "A method for accurate pH mapping with chemical exchange saturation transfer (CEST) MRI," *Contrast Media & Molecular Imaging*, vol. 11, no. 3, pp. 195–202, 2016. CMMI-15-0054.R1.

[13] J. Ren, R. Trokowski, S. Zhang, C. R. Malloy, and A. D. Sherry, "Imaging the tissue distribution of glucose in livers using a PARACEST sensor," *Magnetic Resonance in Medicine*, vol. 60, no. 5, pp. 1047–1055, 2008.

[14] K. W. Y. Chan, M. T. McMahon, Y. Kato, G. Liu, J. W. M. Bulte, Z. M. Bhujwalla, D. Artemov, and P. C. M. van Zijl, "Natural D-glucose as a biodegradable MRI contrast agent for detecting cancer," *Magnetic Resonance in Medicine*, vol. 68, no. 6, pp. 1764–1773, 2012.

[15] M. Haris, K. Cai, A. Singh, H. Hariharan, and R. Reddy, "In vivo mapping of brain myo-inositol," *NeuroImage*, vol. 54, no. 3, pp. 2079 – 2085, 2011.

[16] W. Ling, R. R. Regatte, G. Navon, and A. Jerschow, "Assessment of glycosaminoglycan concentration in vivo by chemical exchange-dependent saturation transfer (gagCEST)," *Proceedings of the National Academy of Sciences*, vol. 105, no. 7, pp. 2266–2270, 2008.

[17] B. Schmitt, Štefan Zbýň, D. Stelzeneder, V. Jellus, D. Paul, L. Lauer, P. Bachert, and S. Trattnig, "Cartilage quality assessment by using glycosaminoglycan chemical exchange saturation transfer and 23Na MR imaging at 7 T," *Radiology*, vol. 260, no. 1, pp. 257–264, 2011. PMID: 21460030.

[18] F. Kogan, M. Haris, A. Singh, K. Cai, C. Debrosse, R. P. R. Nanga, H. Hariharan, and R. Reddy, "Method for high-resolution imaging of creatine in vivo using chemical exchange saturation transfer," *Magnetic Resonance in Medicine*, vol. 71, no. 1, pp. 164–172, 2014.

[19] D. L. Longo, A. Bartoli, L. Consolino, P. Bardini, F. Arena, M. Schwaiger, and S. Aime, "In vivo imaging of tumor metabolism and acidosis by combining PET and MRI-CEST pH imaging," *Cancer Research*, vol. 76, no. 22, pp. 6463–6470, 2016.

[20] K. A. Davis, R. P. R. Nanga, S. Das, S. H. Chen, P. N. Hadar, J. R. Pollard, T. H. Lucas, R. T. Shinohara, B. Litt, H. Hariharan, M. A. Elliott, J. A. Detre, and R. Reddy,

"Glutamate imaging (GluCEST) lateralizes epileptic foci in nonlesional temporal lobe epilepsy," *Science Translational Medicine*, vol. 7, no. 309, pp. 309ra161–309ra161, 2015.

[21] M. Haris, K. Nath, K. Cai, A. Singh, R. Crescenzi, F. Kogan, G. Verma, S. Reddy, H. Hariharan, E. R. Melhem, and R. Reddy, "Imaging of glutamate neurotransmitter alterations in Alzheimer's disease," *NMR in Biomedicine*, vol. 26, no. 4, pp. 386–391, 2013.

[22] H. Mehrabian, K. L. Desmond, H. Soliman, A. Sahgal, and G. J. Stanisz, "Differentiation between radiation necrosis and tumor progression using chemical exchange saturation transfer," *Clinical Cancer Research*, vol. 23, no. 14, pp. 3667–3675, 2017.

[23] B. S. Meldrum, "Glutamate as a neurotransmitter in the brain: Review of physiology and pathology," *The Journal of Nutrition*, vol. 130, no. 4, p. 1007, 2000.

[24] M. R. Hynd, H. L. Scott, and P. R. Dodd, "Glutamate-mediated excitotoxicity and neurodegeneration in Alzheimer's disease," *Neurochemistry International*, vol. 45, no. 5, pp. 583 – 595, 2004.

[25] I. R. Stojanovic, M. Kostic, and S. Ljubisavljevic, "The role of glutamate and its receptors in multiple sclerosis," *Journal of Neural Transmission*, vol. 121, pp. 945–955, Aug 2014.

[26] B. Meldrum, "The role of glutamate in epilepsy and other cns disorders," vol. 44, pp. S14–23, 12 1994.

[27] T. Thiel, M. Czisch, G. K. Elbel, and J. Hennig, "Phase coherent averaging in magnetic resonance spectroscopy using interleaved navigator scans: Compensation of motion artifacts and magnetic field instabilities," *Magnetic Resonance in Medicine*, vol. 47, no. 6, pp. 1077–1082, 2002.

[28] A. T. Hess, M. Dylan Tisdall, O. C. Andronesi, E. M. Meintjes, and A. J. W. van der Kouwe, "Real-time motion and B0 corrected single voxel spectroscopy using volumetric navigators," *Magnetic Resonance in Medicine*, vol. 66, no. 2, pp. 314–323, 2011.

[29] A. T. Hess, O. C. Andronesi, M. Dylan Tisdall, A. Gregory Sorensen, A. J. W. van der Kouwe, and E. M. Meintjes, "Real-time motion and B0 correction for localized adi-

abatic selective refocusing (LASER) MRSI using echo planar imaging volumetric navigators," *NMR in Biomedicine*, vol. 25, no. 2, pp. 347–358, 2012.

[30] E. Heckova, M. Považan, B. Strasser, P. Krumpolec, P. Hnilicová, G. J. Hangel, P. A. Moser, O. C. Andronesi, A. J. van der Kouwe, P. Valkovic, B. Ukropcova, S. Trattnig, and W. Bogner, "Real-time correction of motion and imager instability artifacts during 3D γ-aminobutyric acid–edited MR spectroscopic imaging," *Radiology*, p. 170744, 2017. PMID: 28957645.

[31] "SDBSWeb." `http://sdbs.db.aist.go.jp/sdbs/cgi-bin/direct_frame_disp.cgi?sdbsno=899`. Accessed: 2017-12-17.

[32] F. Bloch, "Nuclear induction," *Phys. Rev.*, vol. 70, pp. 460–474, Oct 1946.

[33] G. A. Morris and R. Freeman, "Enhancement of nuclear magnetic resonance signals by polarization transfer," *Journal of the American Chemical Society*, vol. 101, no. 3, pp. 760–762, 1979.

[34] M. Zaiss and P. Bachert, "Chemical exchange saturation transfer (CEST) and MR Z -spectroscopy in vivo : a review of theoretical approaches and methods," *Physics in Medicine & Biology*, vol. 58, no. 22, p. R221, 2013.

[35] S. Gruber, E. Heckova, B. Strasser, M. Povazan, G. J. Hangel, L. Minarikova, S. Trattnig, and W. Bogner, "Mapping an extended neurochemical profile at 3 and 7 t using accelerated high-resolution proton magnetic resonance spectroscopic imaging," *Investigative Radiology*, vol. 52, no. 10, 2017.

[36] H. M. McConnell, "Reaction rates by nuclear magnetic resonance," *The Journal of Chemical Physics*, vol. 28, no. 3, pp. 430–431, 1958.

[37] M. Zaiss, Z. Zu, J. Xu, P. Schuenke, D. F. Gochberg, J. C. Gore, M. E. Ladd, and P. Bachert, "A combined analytical solution for chemical exchange saturation transfer and semi-solid magnetization transfer," *NMR in Biomedicine*, vol. 28, no. 2, pp. 217–230, 2015. NBM-14-0190.R2.

[38] P. C. M. van Zijl and N. N. Yadav, "Chemical exchange saturation transfer (CEST): What is in a name and what isn't?," *Magnetic Resonance in Medicine*, vol. 65, no. 4, pp. 927–948, 2011.

[39] M. Zaiss, J. Windschuh, S. Goerke, D. Paech, J.-E. Meissner, S. Burth, P. Kickingereder, W. Wick, M. Bendszus, H.-P. Schlemmer, M. E. Ladd, P. Bachert, and A. Radbruch, "Downfield-noe-suppressed amide-cest-mri at 7 tesla provides a unique contrast in human glioblastoma," *Magnetic Resonance in Medicine*, vol. 77, no. 1, pp. 196–208, 2017.

[40] M. Zaiss, M. Schnurr, and P. Bachert, "Analytical solution for the depolarization of hyperpolarized nuclei by chemical exchange saturation transfer between free and encapsulated xenon (HyperCEST)," *The Journal of Chemical Physics*, vol. 136, no. 14, p. 144106, 2012.

[41] M. Zaiss and P. Bachert, "Exchange-dependent relaxation in the rotating frame for slow and intermediate exchange – modeling off-resonant spin-lock and chemical exchange saturation transfer," *NMR in Biomedicine*, vol. 26, no. 5, pp. 507–518, 2013.

[42] J. Zhou, J.-F. Payen, D. A. Wilson, R. J. Traystman, and P. C. M. van Zijl, "Using the amide proton signals of intracellular proteins and peptides to detect pH effects in MRI," *Nature Medicine*, vol. 9, pp. 1085 EP –, Jul 2003.

[43] M. Kim, J. Gillen, B. A. Landman, J. Zhou, and P. C. van Zijl, "Water saturation shift referencing (WASSR) for chemical exchange saturation transfer (CEST) experiments," *Magnetic Resonance in Medicine*, vol. 61, no. 6, pp. 1441–1450, 2009.

[44] M. Zaiß, B. Schmitt, and P. Bachert, "Quantitative separation of CEST effect from magnetization transfer and spillover effects by Lorentzian-line-fit analysis of Z-spectra," *Journal of Magnetic Resonance*, vol. 211, no. 2, pp. 149 – 155, 2011.

[45] A. N. Dula, L. R. Arlinghaus, R. D. Dortch, B. E. Dewey, J. G. Whisenant, G. D. Ayers, T. E. Yankeelov, and S. A. Smith, "Amide proton transfer imaging of the breast at 3 T: Establishing reproducibility and possible feasibility assessing chemotherapy response," *Magnetic Resonance in Medicine*, vol. 70, no. 1, pp. 216–224, 2013.

[46] P. Schuenke, J. Windschuh, V. Roeloffs, M. E. Ladd, P. Bachert, and M. Zaiss, "Simultaneous mapping of water shift and B1 (WASABI)—application to field-inhomogeneity correction of CEST MRI data," *Magnetic Resonance in Medicine*, vol. 77, no. 2, pp. 571–580, 2017.

[47] E. Poblador Rodriguez, P. Moser, B. Dymerska, S. Trattnig, and W. Bogner, "Interleaved B0-mapping during dynamic Creatine-CEST for correction of temporarily fluctuating B0 inhomogeneities during plantar flexion exercise at 7T," in *25th ISMRM Annual Meeting and Exhibition 2017 and 26th SMRT Annual Meeting 2017*, no. 3758, International Society for Magnetic Resonance in Medicine, 2017.

[48] J. Windschuh, M. Zaiss, J.-E. Meissner, D. Paech, A. Radbruch, M. E. Ladd, and P. Bachert, "Correction of B1-inhomogeneities for relaxation-compensated CEST imaging at 7T," *NMR in Biomedicine*, vol. 28, no. 5, pp. 529–537, 2015. NBM-14-0251.R2.

[49] U. Klose, "Mapping of the radio frequency magnetic field with a MR snapshot FLASH technique," *Medical Physics*, vol. 19, no. 4, pp. 1099–1104, 1992.

[50] S. Chung, D. Kim, E. Breton, and L. Axel, "Rapid B1+ mapping using a preconditioning RF pulse with TurboFLASH readout," *Magnetic Resonance in Medicine*, vol. 64, no. 2, pp. 439–446, 2010.

[51] M. L. Wood and R. M. Henkelman, "MR image artifacts from periodic motion," *Medical Physics*, vol. 12, no. 2, pp. 143–151, 1985.

[52] W. Van de, Lemahieu, and Achten, "Magnetic resonance imaging and the reduction of motion artifacts: review of the principles.," *Technology & Health Care*, vol. 5, no. 6, p. 419, 1997.

[53] T. Shah, L. Lu, K. M. Dell, M. D. Pagel, M. A. Griswold, and C. A. Flask, "CEST-FISP: A novel technique for rapid chemical exchange saturation transfer MRI at 7 T," *Magnetic Resonance in Medicine*, vol. 65, no. 2, pp. 432–437, 2011.

[54] K. Lu, T. T. Liu, and M. Bydder, "Optimal phase difference reconstruction: comparison of two methods," *Magnetic Resonance Imaging*, vol. 26, no. 1, pp. 142 – 145, 2008.

[55] F. C. Wermter, C. Bock, and W. Dreher, "Investigating GluCEST and its specificity for pH mapping at low temperatures," *NMR in Biomedicine*, vol. 28, no. 11, pp. 1507–1517, 2015. NBM-15-0090.R2.

[56] S. Walker-Samuel, R. Ramasawmy, F. Torrealdea, M. Rega, V. Rajkumar, S. P. Johnson, S. Richardson, M. Gonçalves, H. G. Parkes, E. Årstad, D. L. Thomas, R. B. Pedley, M. F. Lythgoe, and X. Golay, "In vivo imaging of glucose uptake and metabolism in tumors," *Nature Medicine*, vol. 19, pp. 1067 EP –, Jul 2013.

[57] X. Xu, K. W. Chan, L. Knutsson, D. Artemov, J. Xu, G. Liu, Y. Kato, B. Lal, J. Laterra, M. T. McMahon, and P. C. van Zijl, "Dynamic glucose enhanced (DGE) MRI for combined imaging of blood–brain barrier break down and increased blood volume in brain cancer," *Magnetic Resonance in Medicine*, vol. 74, no. 6, pp. 1556–1563, 2015.

[58] T. K. Stevens, K. K. Palaniappan, R. M. Ramirez, M. B. Francis, D. E. Wemmer, and A. Pines, "HyperCEST detection of a 129Xe-based contrast agent composed of cryptophane-A molecular cages on a bacteriophage scaffold," *Magnetic Resonance in Medicine*, vol. 69, no. 5, pp. 1245–1252, 2013.